The Teena Zn-Pb Deposit (McArthur Basin, Australia). Part II: Carbonate Replacement Sulfide Mineralization During Burial Diagenesis— Implications for Mineral Exploration

J. M. Magnall,[1,†] N. Hayward,[2] S. A. Gleeson,[1,3] A. Schleicher,[1] I. Dalrymple,[2] R. King,[4] and N. Mahlstadt[1]

[1]GFZ German Research Centre for Geosciences, 14473 Potsdam, Germany

[2]Teck Australia Pty. Ltd., P.O. Box 1677, Western Australia 6872, Australia

[3]Institute of Geological Sciences, Freie Universität Berlin, Malteserstrasse, 74-100, Berlin 12249, Germany

[4]De Grey Mining Ltd., 22 Railway Road, Subiaco, Western Australia 6008, Australia

Abstract

The Teena Zn-Pb deposit is located in the Carpentaria Zn Province (Australia), which contains some of the largest clastic dominant (CD-type) massive sulfide Zn-Pb deposits in the world. The timing of the main stage of hydrothermal sulfide mineralization in the Teena subbasin is constrained to the midstage of burial diagenesis, during a period of short-lived regional extension. To distinguish hydrothermal alteration from spatially and temporally overlapping burial diagenetic alteration, and to establish the primary controls on hydrothermal mass transfer, it is necessary to evaluate the various foot- and hanging-wall alteration assemblages that formed between early- (eogenesis) and late- (mesogenesis) stage diagenesis. To achieve this, we have statistically evaluated a large lithogeochemistry dataset (n >2,500) and selected a subset (n = 65) of representative samples for detailed mineralogical (X-ray diffraction, illite crystallinity) and petrographic (scanning electron microscopy) analyses; hyperspectral core imaging data were then used to upscale key paragenetic observations.

We show that sulfide mineralization was predated by multiple diagenetic alteration assemblages, including stratiform pyrite, dolomite nodules and cement, disseminated hematite and authigenic K-feldspar. These assemblages formed during eogenesis in multiple subbasins across the broader McArthur Basin and are not part of the synmineralization alteration footprint. Whereas pyrite and dolomite formed primarily from the in situ degradation of organic matter, feldspar authigenesis was the product of K metasomatism that was focused along permeable coarse-grained volcaniclastic sandstone beds within the host-rock sequence. The immature volcaniclastic input is broadly representative of the siliciclastic compositional end member in the subbasin, which formed the protolith for phyllosilicate (illite, phengite, chlorite) formation during burial diagenesis. There is no evidence of extensive phyllosilicate alteration in any of the geochemical, mineralogical (illite crystallinity), or petrographic datasets, despite some evidence of K-feldspar replacement by sphalerite in the Lower and Main mineralized lenses. Rather, the high Zn grades formed via dolomite replacement, which is resolvable from a chemical mass balance analysis and consistent with petrographic observations.

There are significant exploration implications associated with carbonate-replacement sulfide mineralization during mesogenesis: (1) the capacity for secondary porosity generation in the host rock is as important as its sulfate-reducing capacity; (2) hydrothermal mineralization has a short-range cryptic lateral and vertical synmineralization alteration footprint due to acid neutralization by a carbonate-rich protolith; and (3) the distribution and chemistry of premineralization phases (e.g., pyrite, dolomite nodules) cannot be directly related to the mineralization footprint, which is localized to the 4th-order subbasin scale. Future exploration for this deposit style should therefore be focused on identifying units that contain a mixture of organic carbon and carbonate in the protolith, at favorable stratigraphic redox boundaries, and proximal to feeder growth faults.

Introduction

Some of Earth's largest base metal resources are associated with clastic-dominant (CD-type) massive sulfide deposits (Mudd et al., 2017). These mineral systems can be very large (10^2 Mt ore) and high grade (>10% combined Zn + Pb), yet they are difficult to predict and detect in the terrestrial rock record. The capacity of exploration programs to detect mineralized rocks is dependent on accurate mineral system models that describe the alteration footprint of deposits. The mineralogical expression of hydrothermal alteration is primarily controlled by the mineralogical composition of the protolith and fluid chemistry; however, reliable constraints for both param-

eters are commonly lacking in CD-type systems, due to the absence of reliable fluid inclusion data and modifications from metamorphism and deformation, as well as hypogene and supergene alteration. Compared to other resources in sedimentary basins (e.g., hydrocarbons), therefore, exploration models for CD-type deposits are relatively underdeveloped.

The prevailing model for many CD-type deposits involves sedimentary exhalative (SEDEX) processes, whereby layered sulfide minerals formed when hydrothermal fluids vented into sulfidic (euxinic) seawater (e.g., Goodfellow et al., 1993). In the SEDEX model, sulfide minerals precipitate directly from seawater, resulting in laterally extensive orebodies that are conformable (stratiform/stratabound) with the carbonaceous mudstone host rock. In the SEDEX model, highly reduc-

†Corresponding author: e-mail, magnall@gfz-potsdam.de

ing depositional environments are considered to have been favorable for ore formation due to the in situ availability of reduced sulfur. The use of modern reduced settings (e.g., Black Sea) as analogues for ancient basins hosting SEDEX deposits means that regional exploration targets are limited to parts of the sedimentary record where there is evidence of water mass restriction and stagnation (e.g., Goodfellow, 1987; Turner, 1992). More local exploration targets are then limited to the most reduced euxinic depositional facies (e.g., Goodfellow and Lydon, 2007). As hydrothermal venting is considered to have resulted in widespread trace element dispersion, studies have tended to focus on sedimentary pyrite as an archive of trace element anomalism around SEDEX deposits (e.g., Mukherjee and Large, 2017).

Contrary to the SEDEX model, many researchers have made petrographic arguments that CD-type deposits formed via replacement processes during diagenesis (Grondijs and Schouten, 1937; Williams, 1978; Magnall et al., 2020a; Spinks et al., 2021). Furthermore, recent studies have shown that the protolith of CD-type deposits accumulated under a range of depositional redox conditions, albeit with minimal evidence of prolonged euxinia (Reynolds et al., 2015; Magnall et al., 2018, 2020b). Where CD-type deposits are formed via subseafloor replacement it is necessary to evaluate the spatial and temporal relationships between hydrothermal and diagenetic processes. Moreover, two questions are particularly important in the context of subseafloor replacement: (1) What were the main factors controlling porosity and permeability evolution in the subsurface? (2) How can we distinguish a hydrothermal alteration footprint from the burial diagenetic footprint to help target future discoveries?

Before evaluating such questions, it is necessary to provide a precise definition of diagenesis. In the broadest terms, diagenesis includes the physical- and fluid-mediated chemical transformations that take place as highly porous sediments become less porous, coherent rocks (Meunier, 2005). The evolution of sediments to rocks progresses from ambient conditions at the sediment water interface (SWI) through to sub-greenschist facies metamorphism during deeper burial (5°–300°C; Milliken, 2003), resulting in variable and overlapping nomenclature for different parts of the process. This paper uses the classification of Schmidt and McDonald (1979), in which diagenesis in clastic sediments and sedimentary rocks is subdivided into the following three stages:

1. Eogenesis (early), during which the composition of sediment pore fluids is controlled primarily by seawater chemistry and low-temperature (<50°C), biologically mediated reactions involved in organic matter degradation (e.g., Morad et al., 2000). By-products of organic matter degradation include alkalinity and reduced sulfur, which can result in the formation of carbonate and pyrite. The formation of primary dolomite (i.e., direct precipitation on the seafloor or in early cements) during some periods of Earth history may also be linked to seawater chemistry (e.g., Proterozoic; Tucker, 1982; Hood et al., 2011). Other examples of open-system mass transfer during eogenesis include the infiltration of meteoric fluids, seawater, and refluxing brine (Worden and Burley, 2003); however, in carbonate platform environments, eogenetic carbonate cementation may

also result in porosity destruction and a reduction in overall reservoir quality (Ehrenberg, 2006).

2. Mesogenesis (middle), during which dehydration of clay minerals commences and when compaction and cementation during burial result in a transition toward closed-system conditions. Any large-scale subsurface mass transfer during this stage requires a combination of secondary porosity creation and high fluid fluxes to maintain undersaturation of occluding mineral phases (Bjørlykke and Jahren, 2012).

3. Telogenesis, which is associated with the reintroduction of meteoric fluids during uplift and exposure (e.g., Burley et al., 1985).

The composition of detrital input provides a 1st-order control on the mineralogical transformations that occur during clastic diagenesis (Bjørlykke, 2014). The solubility of most mineral phases during diagenesis is strongly dependent on pH, meaning that organic matter maturation and the in situ generation of organic acid play an important role in many mineral transformations (Smith and Ehrenberg, 1989; Helgeson et al., 1993). Clay minerals and organic matter both follow characteristic prograde reaction sequences during mesogenesis (Merriman, 2005); for example, inherited (detrital) or neoformed smectite loses structurally bound water and transforms to illite/smectite (Środoń, 1999), then to illite, phengite, and muscovite (Bjørlykke, 1998; McKinley et al., 2009). Organic matter maturity indicators, typically generated via Rock Eval techniques or vitrinite reflectance, can also provide valuable information on the temperature regime of mesogenesis. At temperatures between 80° and 180°C, kerogen undergoes primary cracking (10 and 90% conversion, respectively) to bitumen and gas (Bernard and Horsfield, 2014). This diagenetic stage is also referred to as catagenesis, which is a subset of mesogenesis. Depending on heating rate, the secondary conversion of bitumen to oil and gas then begins around 150°C. Generated gas may be stored in porosity, adsorbed onto kerogen and clays, or dissolved in kerogen and pyrobitumen. In thermally mature gas shales, most intramineral pore spaces are filled with bitumen, which shows that they were once interconnected to a degree to allow migration of precursor hydrocarbons.

Finding a location where diagenetic and hydrothermal processes can be evaluated in the structural context of subbasin evolution is challenging, given the tectonic and metamorphic overprint that has affected many of the largest CD-type deposits (e.g., Blevings et al., 2013; Martel, 2017). This study addresses the Teena deposit, which is the most recent Zn discovery in the Carpentaria Zn Province (Fig. 1A). The Teena deposit is in the Teena subbasin, which is part of the McArthur Basin (Fig. 1A). Similar to the HYC deposit located <10 km away (Fig. 1B), the Teena deposit is unmetamorphosed and has been affected by only very weak orogenesis (Hayward et al., 2021). This part of the McArthur Basin, therefore, is one of the best natural laboratories in which to study the diagenetic and hydrothermal evolution of a mineralized subbasin.

In Part I of this study, Hayward et al., (2021) developed a structural model for the Teena subbasin and described the occurrence of subseafloor replacement-style sulfide mineralization at three separate stratigraphic levels. Mineralization styles include two higher grade stratiform lenses (Lower and Main) of massive sulfide and two footwall intervals of lower grade
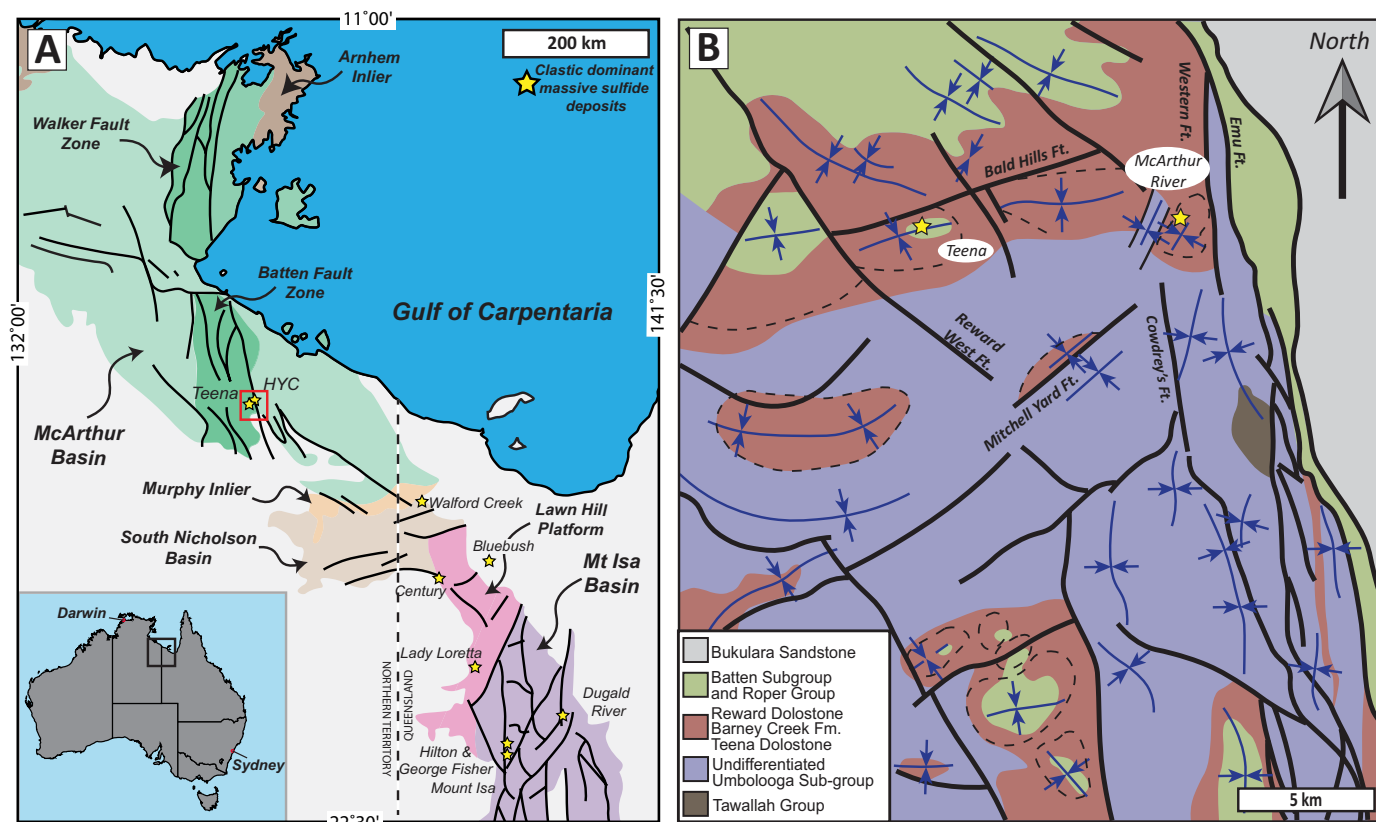
Fig 1. (A). The geographic extent of the Isa superbasin, which includes the respective Mt. Isa and McArthur River Basins. The Teena and McArthur River (HYC) deposits (yellow stars) are located within the Batten fault zone that makes up the Carpentaria Zn Province. The red box outlines the area shown in (B). (B). The geology of the southern Batten fault zone where the Teena and McArthur River (HYC) deposits are located within fault-bound subbasins (enclosed by dashed lines). Arrows and adjoining lines mark the respective dip direction of fold limbs and fold axial traces. Modified from Hayward et al. (2021) and McGoldrick et al. (2010).

stratiform mineralized rocks and stratabound hydrothermal mineralized dolostones (Hayward et al., 2021). This contribution, following the structural model for subbasin development presented in Part I (Hayward et al., 2021), evaluates the primary controls on diagenetic and hydrothermal mass transfer during subbasin development; in particular, the pre-, syn- and postmineralization mineral assemblages that are directly associated with stratabound and stratiform mineralization in the clastic sedimentary rocks of the Lower and Main lenses. To ensure that datasets are linked effectively across different scales, we have statistically evaluated a large bulk-rock lithogeochemistry database to ensure the samples selected for petrography and detailed mineralogical analysis (X-ray diffractometry and illite crystallinity) are compositionally representative of the subbasin; hyperspectral core imaging was then used to upscale the petrographic evidence. In combination with Part I, this work facilitates development of an internally consistent model that describes where, when, and how mineralization occurred in the Lower and Main lenses at Teena.

Geologic Background

Geodynamic setting and basin architecture

The Isa Superbasin, which is comprised of a pair of 2nd-order (10^3 km^2) basins referred to as the Mt. Isa and McArthur

Basins, formed during a period of lithospheric extension between 1.82 and 1.58 Ga (Southgate et al., 2000). This long-lived period of extension was interrupted by episodes of inversion, uplift, and erosion, which define three consecutive cycles of basin evolution (Leichardt, Calvert, and Isa). The stress regimes that controlled evolution of the Isa Superbasin have been linked to a long-lived subduction zone on the southern margin (Southgate et al., 2000; Betts et al., 2006) and a passive continental margin that was developed along the eastern margin (Betts et al., 2016). The N-trending Walker and Batten fault zones were particularly important for accommodating strain and are major features in the structural architecture of the McArthur Basin (Fig. 1). These fault zones contain several 3rd- (10^2 km^2) and 4th-order (10^1 km^2) subbasins, and some of the latter are host to CD-type deposits (Fig. 1B). Closure of the 1st-order Isa Superbasin has been variously linked to subduction and terrane collisions farther east and south after 1640 Ma and was followed by the Isan orogeny between 1600 and 1500 Ma (Betts et al., 2006; Srimgeour, 2006). In the McArthur Basin, the tectonic and metamorphic grade associated with the Isan orogeny is generally quite low, meaning that some of the oldest hydrocarbon source rocks of Precambrian age are well preserved and essentially unmetamorphosed (Jackson et al., 1987; Crick et al., 1988; Baruch et al., 2015).

Stratigraphy of the McArthur Basin

The McArthur Basin contains a 5- to 15-km-thick succession of mixed carbonate and siliciclastic rocks that are intercalated with bimodal volcanic rocks (Plumb, 1979; Jackson et al., 1987; Rawlings, 1999). There are two stratigraphic frameworks for the McArthur Basin based on lithostratigraphy (e.g., Jackson et al., 1987; Rawlings, 1999) or sequence stratigraphy (e.g., Southgate et al., 2000). The advantage of the sequence stratigraphic framework is that it correlates sequences of equivalent age that may have differing composition. This is particularly important for correlations made at the 1st-order basin scale, and for differentiation of 3rd- and 4th-order sequences and parasequences at the district and deposit scale.

The Leichardt, Calvert, and Isa Superbasin cycles contain a series of unconformity-bound depositional supersequences (Southgate et al., 2000). Many of the Carpentaria CD-type Zn deposits are hosted in the lowermost Isa Superbasin cycle (Large et al., 2005), which represents the sag phase of rift development (Betts et al., 2003). The River Supersequence (1640–1630 Ma) is subdivided into 3rd-order depositional cycles that span approximately 1 to 5 m.y. (Fig. 2). The Barney Creek Formation of the Barney Creek depositional cycle is host to the HYC, Teena, and Myrtle deposits in the Batten fault zone (Hayward et al., 2021).

The Teena Dolostone is the oldest unit in the Barney Creek Formation and is composed of shallow-water stromatolitic dolostone, cross-laminated dolarenite, and evaporites that formed in a shallow subtidal to supratidal environment (Jackson et al., 1987; Kunzmann et al., 2019). The overlying W-Fold Shale Member is comprised of interbedded thin dolomitic sandstones and siltstones that contain a variety of dolomite nodules. The W-Fold Shale Member also preserves patchy green and red alteration and is interpreted to have been deposited in an intertidal to shallow subtidal environment (Kunzmann et al., 2019). The overlying Lower HYC Pyritic Shale Member (Lower HYC unit) is a dolomitic, variably carbonaceous silt- and mudstone that was deposited below the storm wave base. The W-Fold Shale Member and Lower HYC Pyritic Shale Member both contain slump folds, minor sandstone beds, minor sedimentary breccias (restricted to Lower HYC), and significant stratigraphic thickening proximal to fault-bound subbasin margins (Hayward et al., 2021). The overlying Middle HYC Pyritic Shale Member (Middle HYC unit) contains similar lithologies to the underlying Lower HYC Pyritic Shale Member, but with less dolomite and silt and more organic matter and pyrite; it is interpreted to have formed in the deepest water conditions present during deposition of the Barney Creek Formation (McGoldrick et al., 2010; Kunzmann et al., 2019). Relative to the underlying Lower and Middle Members, the Upper HYC Pyritic Shale Member (Upper HYC unit) contains a greater proportion of siltstone and sandstone beds and becomes more dolomitic as the unit transitions into the overlying Reward Dolostone. The Reward Dolostone is the uppermost unit of the Barney Creek Formation and is unconformably overlain by the Lynott Formation. The overall age of the Barney Creek Formation is constrained by the youngest detrital U-Pb zircon ages of 1639 ± 6 and 1636 ± 4 Ma for the respective underlying (Teena Dolostone) and overlying (Lynott Formation) lithologic units (Page et al., 2000). Additionally, tuffaceous beds within the Barney Creek Formation contain zircons with ages of 1638 ± 7, 1639 ± 3, and 1640 ± 3 Ma (Page and Sweet, 1998).

Two 3rd-order transgressive-regressive (T-R) sequences (B1 and B2) can be correlated across the Batten fault zone (Kunzmann et al., 2019). The transgressive and regressive systems tracts (RST and TST) are separated by maximum flooding surfaces (MFS) (Fig. 2), which is marked by particularly high concentrations of organic carbon and pyrite and by peaks in the gamma ray logs (Kunzmann et al., 2019). In the Teena subbasin, the pyrite in the B1 (MFS) records highly positive $\delta^{34}S$ values that are interpreted to represent the development of euxinic conditions during high levels of localized productivity in the basin (Magnall et al., 2020b). The location of the B1 and B2 MFSs have been used as stratigraphic markers for correlating the base of the Middle and Upper HYC units between drill cores in the Teena subbasin (Magnall et al., 2020b).

Geology of the Teena and McArthur River (HYC) deposits

The Teena and McArthur River (HYC) deposits are located in 4th-order subbasins that are located in the 3rd-order Hot Spring-Emu subbasin (Fig. 1B). Syndepositional tectonic activity had a major impact on the Barney Creek Formation at the 4th-order scale, and the main structures that controlled sedimentation and hydrothermal activity in the Teena subbasin were the easterly striking Jabiru and Bald Hills faults (Fig. 3; Hayward et al., 2021). Similarly, in the subbasin that is host to the McArthur River (HYC) deposit the Emu and Western faults had a major influence on sedimentation and hydrothermal activity (Ireland et al., 2004; McGoldrick et al., 2010).

There are multiple high-grade stratiform mineralized intervals in the Lower HYC unit in the Teena and HYC subbasins. In the Teena subbasin, the highest grades are located in two intervals (Main and Lower lenses) that are separated by graded volcaniclastic sandstone beds; additionally, there are also footwall zones containing low-grade stratiform sulfides and hydrothermal dolomite (HTD) with interstitial sphalerite in the underlying W-Fold Shale Member (Hayward et al., 2021). In the HYC subbasin there are eight intervals containing stratiform sulfides with high Zn and Pb grades that are separated by coarse-grained mass flow deposits (Large et al., 1998; Ireland et al., 2004).

At the Teena deposit the stratiform sulfides consist primarily of fine-grained sphalerite cement within pyritic, dolomitic, carbonaceous siltstone (e.g., Fig. 4A; Main lens), or coarser grained sphalerite intergrown with dolomite nodules (e.g., Fig. 4B; Lower lens). Both styles of sphalerite are considered to have formed coevally and are referred to as sp1 (Fig. 4D; Hayward et al., 2021). Textural evidence indicates precipitation of sp1 postdated the formation of fine-grained diagenetic pyrite (py1) and nodular dolomite. Sp1 was broadly coeval with the formation of coarser grained spherical aggregates of pyrite enriched in Pb and As (py2; Magnall et al., 2020b). A second generation of red-brown sphalerite (sp2) formed coarse-grained bedding-parallel bands and is commonly spatially associated with dissolution cavities containing quartz-carbonate-sulfide infill (e.g., Fig. 4C). The hydrothermal activity that resulted in sulfide preceipitation in the Lower and Main lenses is considered to have been synchronous with the
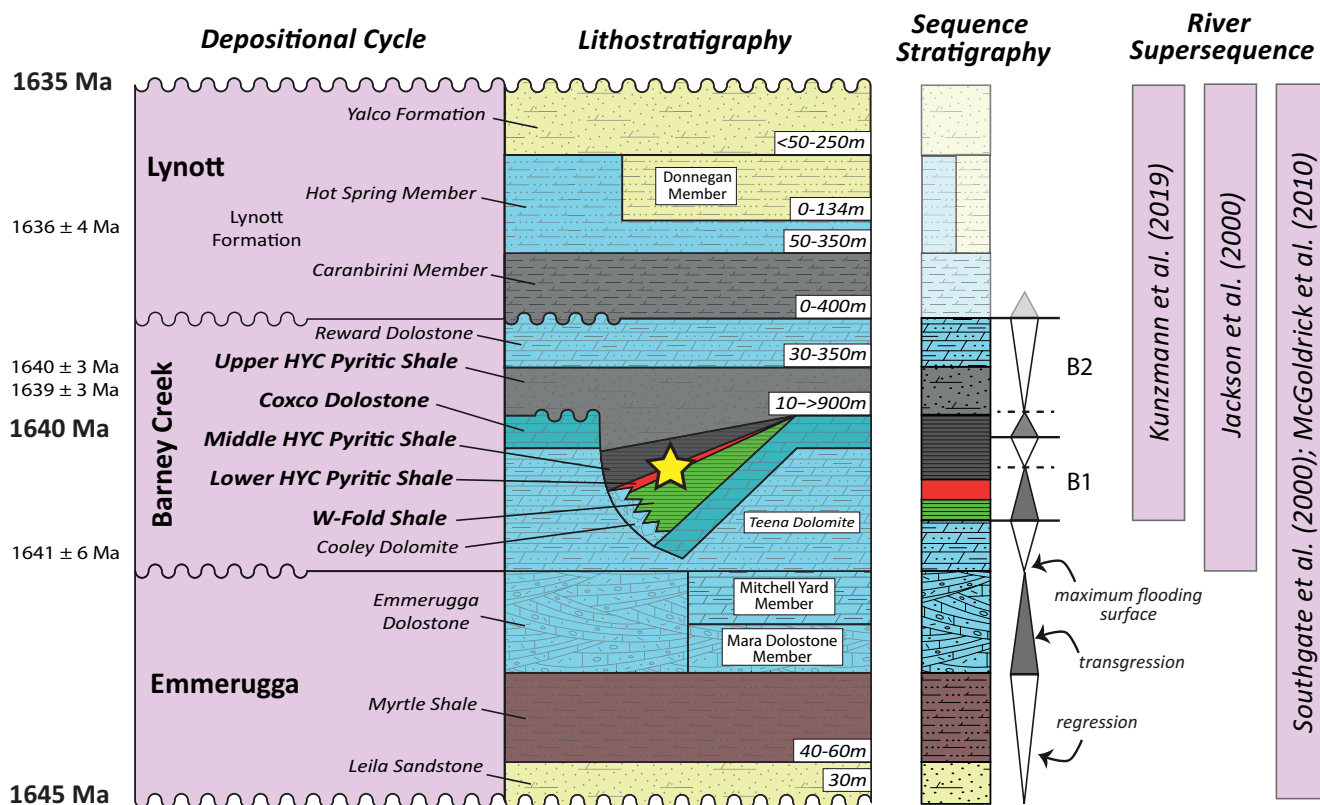
Fig. 2. A chronostratigraphic chart for the River supersequence in the Emu-Hot Springs subbasin. The age constraints and approximate unit thicknesses are compiled from Jackson et al. (1987) and Ahmad et al. (2013). The 3rd-order sequence boundaries are provided by Kunzmann et al. (2019) and represented by triangles that thin toward the maximum flooding surfaces (MFS, B1 and B2). The different interpretations for the start of the River supersequence are labeled on the right-hand side (Kunzmann et al., 2019; Jackson et al., 2000; McGoldrick et al., 2000; Southgate et al., 2000;).

later stages of extension in the subbasin, i.e., syndepositional to the Middle HYC unit (Fig. 4D; Hayward et al., 2021).

The style of stratiform mineralization in the ore lenses of the McArthur River (HYC) deposit is similar to the Lower and Main lenses of the Teena deposit, although there are significantly higher Pb and Ag grades at the McArthur River (HYC) deposit. There has been considerable debate over the sulfide paragenesis at the McArthur River (HYC) deposit, and specifically the relative timing of fine-grained diagenetic pyrite and sphalerite mineralization (summarized by Large et al., 1998). For example, previous researchers either favor models in which the bulk of the Zn mineralization is syn-py1, consistent with a SEDEX model (e.g., Large et al., 1998; Ireland et al., 2004) or post-py1, which is consistent with subseafloor replacement (Williams, 1978; Eldridge et al., 1993; Spinks et al., 2021).

In the Teena subbasin there is a third zone containing lower grade stratiform and stratabound sulfides in the middle of the footwall W-Fold Shale Member (Hayward et al., 2021). This mineralized zone formed in association with stratabound lenses of HTD via both replacement and dissolution and infill of dolomitic, carbonaceous siltstone. The HTD lenses preserve multiple stages of dissolution and cavity infill, in which coarse-bladed dolomite fans are cemented by interstitial sphalerite, dolomite, and quartz, which are then crosscut by late-stage stockworks of ankerite veins (Hayward et al., 2021). The cavity infill zones are interspersed among broader stratabound lenses of massive dolomite replacement, ankerite veining, and

secondary quartz-dolomite recrystallization after dolomite nodules. Low-grade, stratiform mineralization in the W-Fold Shale Member is interpreted to have predated formation of the HTD lenses and is considered to have formed broadly coevally with the Lower and Main lenses; whereas, sulfides in the HTD-style lenses likely formed coevally with the paragenetically late and coarser grained sp2 in the Lower and Main lenses (Fig. 4D). Minor Zn mineralization also occurred in a hydrothermal breccia associated with the Jabiru fault and in synorogenic veins that crosscut the hanging-wall stratigraphy (Hayward et al., 2021).

In addition to the widespread HTD alteration assemblages, Hayward et al (2021) described several hydrothermal vein and fault-related breccia assemblages at the Teena deposit that mostly postdate the main period of sulfide mineralization. These assemblages include ankerite vein stockworks and minor bed-parallel quartz-hematite veins in the footwall sequence, as well as synorogenic quartz-carbonate-sulfide veins in the hanging wall. Unmineralized dolomite-cemented dissolution breccias ("black-matrix" breccias) are also present in the footwall of the Jabiru fault; they appear to be associated with growth fault development during diagenesis and predate deposition of the Upper HYC unit, but their paragenetic timing with respect to Zn mineralization has not yet been determined. Since the focus of this paper is on pre- to synmineralization diagenetic alteration, these late-stage hydrothermal assemblages are not discussed further.
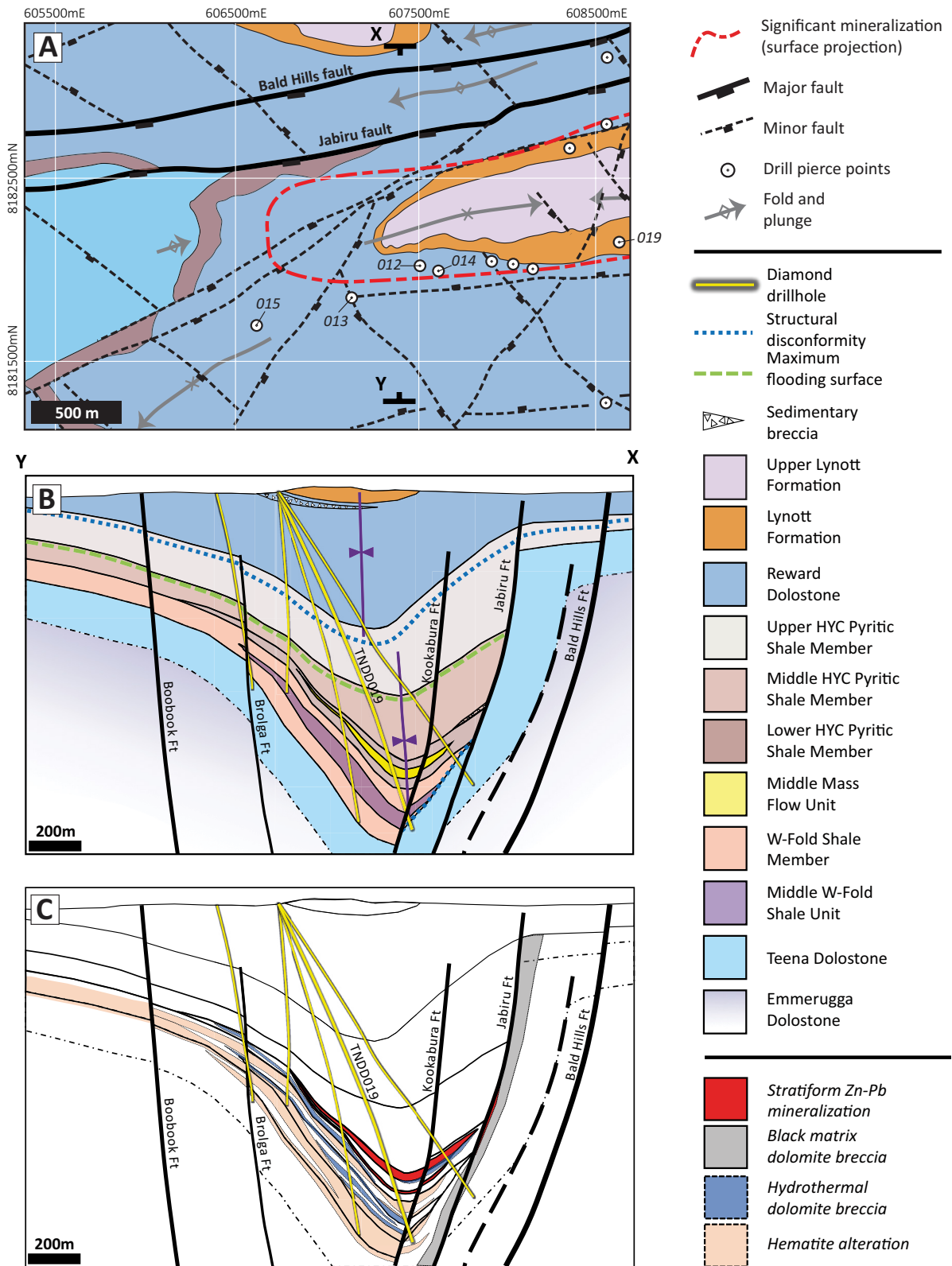
Fig. 3. (A). Interpreted bedrock geologic map of the Teena subbasin showing drill hole collars (white circles) along with the outline of significant Zn-Pb mineralization projected to surface (red dashed line). (B). A geologic cross section through line X-Y (608600 mE, see (A)), showing the main lithologic units and the trace of TNDD019. The Barney Creek Formation is subdivided into the W-Fold Shale Member and Lower, Middle, and Upper HYC Pyritic Shale Members (also referred to as the Lower, Middle, and Upper HYC units in the text). (C). A cross section through the same profile showing the main footwall alteration assemblages.

STRAT. MBR/UNIT	ALTERATION AND MINERALIZATION	Deformation MINERALS	TIMING		
			DE — Early ← Diagenetic → Late		D1 → D4 Orogenic
Lower HYC	Pyritization	Py1a	■		
		Dol nodules	■		
		Py1b	■		
	Stratiform Mineralization	Sp1,Gn1,Py2a,b	■		
		Sp2,Gn2,Py3	■		
W-Fold Shale	Pyritization	Py1a	■		
		Dol nodules	■		
	Stratiform-Min.	Sp1,Gn1,Py2	■		
	Hyd. Dolomite Mineralization	HTD Dol	1 2 3		
		Sp2+,Gn2+,Py3+	1 2 3		
Teena Dolostone	Blk-matrix Brx	Dol	? ▨ ?		
	Fault Brx Min	Sp,Gn,Py	■ ?		
Barney Creek	Vein Sets	Ank Vns		■	
		Qtz-Hem Vns		? ■ ?	
		Qtz-Cb-Sul Vns			■

from Hayward et al. (2021)

Fig. 4. (A). Main lens stratiform mineralization with fine-grained sphalerite cement enveloping remnant mudstone lenses and crosscut by minor late-stage orogenic veinlets. (B). A sample from the Lower lens mineralization in TNDD019, showing dolomite nodules within a carbonaceous and pyritic mudstone (mst). The dolomite nodules show partial selective replacement by sphalerite (sp1). (C). A sample from the Main lens mineralization (TNDD019) that contains both the fine-grained sphalerite (sp1) cement and a strata-bound band of coarse-grained sphalerite (sp2) and galena (gn2) mineralization, as well as quartz + dolomite-filled dissolution cavities (arrows). (D). Paragenesis of mineralization assemblages ordered by timing and stratigraphic position (from Hayward et al., 2021). Ank = ankerite, Cb = carbonate, Dol = dolomite, Hem = hematite, Qtz = quartz, sul = sulfide. Other abbreviations in caption text, above.

Methods

Sampling

This study presents petrographic and geochemical data produced on 14 drill cores from the Teena subbasin (Fig. 3). All these drill cores intersected the Barney Creek depositional cycle and include rocks preserving variable degrees of sulfide mineralization. There were two sampling protocols:

1. The first involved sampling at regular intervals (approximately every 15 m) in order to remove any sampling bias.

The drill core was routinely split in half and 20- to 30-cm-long samples were selected for bulk-rock lithogeochemistry. Continuous lithogeochemistry sampling was conducted where the drill core intersected sulfide-mineralized rock. In total, 2,870 samples were obtained via this sampling methodology.

2. A smaller suite of samples (*n* = 73) was then selected from three drill cores (TNDD015, TNDD012, and TNDD019). These drill cores were selected because they intersected zones affected by weak, moderate, and strong

mineralization, respectively. The samples were smaller in size (<15 cm) and selected to provide greater sampling resolution in the hanging wall of sulfide zones of each drill hole. These samples were also processed for bulk-rock lithogeochemistry.

Drill core logging, petrography, and hyperspectral imaging

All the drill cores described in this study have been logged for lithology, structure, and alteration and mineralization assemblages. Characteristic samples of each unit were further evaluated, using standard petrographic techniques (binocular microscope, transmitted, and reflected light microscopy). The Corescan™ Hyperspectral Core Imager Mark III (HCI-3) was used to map the distribution of carbonate and phyllosilicate phases within continuous intervals of drill core selected from TNDD015 and TNDD022. The HCI-3 is functional across the very near infrared (VNIR) and shortwave infrared (SWIR) electromagnetic spectrum (450–2,500 nm). The HCI-3 has a spectral resolution of 4 nm at a spatial resolution of 0.5 mm.

Inorganic and organic lithogeochemistry

Samples of half or quarter core were sent to Bureau Veritas (Mt. Isa) for major element and assay (Cu, Pb, Zn) analysis (XF01; oxidative fusion followed by XRF analysis). Sample pulps were then analyzed by Bureau Veritas for trace element ICPMS analysis following aqua regia digestion. Carbon and sulfur were analyzed by LECO analysis. Blanks and certified reference materials (CRMs; OREAS131a and 133a, AMIS) were 2021 alongside the samples to monitor data quality. The coefficient of variation for each CRM was less than 5%.

Rock-Eval pyrolysis was conducted by Applied Petroleum Technology (Norway) to provide information about organic matter type, hydrocarbon generation potential, and the thermal maturity of organic material. The method involves heating a powdered sample under inert conditions (helium or nitrogen atmosphere) with increasing temperature. The total amount of generated hydrocarbons was determined (S1 and S2; free hydrocarbons and nonvolatile organic matter, respectively) along with the CO_2 (S3) content. The T_{max} corresponds with the maximum rate of hydrocarbon generation from kerogen cracking. The vitrinite reflectance index (R_o) was calculated by taking the measured T_{max} to a normalized reflectance value using a conversion formula (R_o_calculated = 0.0180 x T_{max} − 7.16; Jarvie et al., 2007).

Principal component analysis

A principal component analysis (PCA) was applied to reduce the dimensionality of the multivariate bulk compositional data into a smaller number of correlated variables (principal components). Unlike factor analysis, there is no probability or significance testing within a PCA, meaning that it is nondependent and assumes all variance is shared. A log transformation of molar concentrations for all the major elements prior to the PCA ensured that inputs with a positively skewed distribution did not impact trends present in the bulk of the dataset. The PCA was performed in ioGAS using the Robust M estimation function, which assigns any outlying samples a low weighting such that they are effectively ignored within the correlation matrix. It was not possible to a perform PCA using the complete array of variables as it does not work on partial

data sets (i.e., if there was no analysis produced for total organic carbon in a sample then the result for this sample would be null). To account for unnecessary data loss associated with samples containing below detection limit concentrations of Pb and Zn, these samples contain imputed values (0.5 * detection limit). In total, 2,705 samples were included in the PCA, which included Al, K, Fe, Mn, Sr, Ca, Mg, Fe, Pb, Zn, and S as input values (mol/kg). Trace elements were excluded from the analysis to avoid additional data loss where there is a high proportion of below detection limit values.

Mass transfer analysis

The bulk mass change and net element transfer associated with sulfide mineralization was evaluated using the Gresens' method (Grant, 1986). This method requires the selection of a suite of immobile element ratios that are calculated from reference values of the altered (mineralized) and unaltered (protolith) rock:

$$C_{i(altered)}/C_{i(unaltered)} \qquad (1)$$

where C_i represents the concentration (ppm) of the immobile element. Immobile elements are neither lost nor gained during alteration and are dispersed along the isocon, which defines the zero net change and is represented by a line that passes through the origin. The slope of the isocon is simply calculated from the median value of equation (1) for the selected immobile element ratios. The net mass change is defined by the slope of the isocon, where >1 indicates bulk mass loss (e.g., mineral dissolution) and <1 indicates bulk mass gain (e.g., mineral precipitation in veins). The bulk mass change (ΔM in %) can be calculated from the following:

$$\Delta M\ (\%) = 100 \times \left[\frac{C_{i(altered)} - C_{i(unaltered)}}{C_{i(unaltered)}} \right]. \qquad (2)$$

The addition or loss of an element (ΔE in %) relative to the reference value is calculated from the following:

$$\Delta E\ (\%) = 100 \times \left[\frac{C_{x(altered)}}{\left(\frac{C_{i(altered)}}{C_{i(unaltered)}} \right) \times C_{x(unaltered)}} - 1 \right], \qquad (3)$$

where $C_{x(altered)}$ and $C_{x(unaltered)}$ are the concentrations of an element of interest in the altered and unaltered samples.

A graphic comparison of $C_{x(altered)}$ and $C_{x(unaltered)}$ can be made by applying a scaling factor, which partly determines the apparent distance each element is located relative to the isocon. To account for this scaling effect it is possible to formulate a modified isocon diagram in which the sum of the square of each element is equal to 1 (Humphris et al., 1998). In the modified isocon diagram, elements with similar behavior will be grouped on one segment of a circle (e.g., immobile elements).

X-ray powder diffractometry

The mineralogy of 63 samples was determined following X-ray powder diffractometry of bulk-rock powders and the clay-size fraction of a subset (n = 37) was analyzed to determine the phyllosilicate minerals present. For quantitative analyses of the bulk mineralogy, a few grams of each sample were crushed and milled to a grain size of <62 μm and then further milled in cyclohexane to <10 μm, using a micronizing

mill, before being dried at 60°C. Randomly oriented powders were transferred into the sample holders which have a grooved circular well. The diffractometer patterns were collected using a PANanalytical Empyrean X-ray Diffractometer operating at 40 kV and 40 mA with Cu-Ka radiation and a three-dimensional pixel detector. The samples were analyzed with the Bragg-Brentano geometry between 4.6° and 75° 2θ and a step-width of 0.02° 2θ. The EVA software (Bruker) was used to initially process the diffraction patterns, where phase identification was made using the search-match function (international center for diffraction data). Phase identification was further informed by bulk-rock lithogeochemistry relationships (e.g., K vs. Al) and SEM. Modeling of the modal mineralogy was then performed using the Rietveld quantitative X-ray diffraction refinement approach (RQXRD) in the software package Profex-BGMN version 3.5.0. For most of the samples it was possible to calculate total carbonate and pyrite from the bulk-rock lithogeochemical data, which was then used as an internal standard for monitoring the accuracy of the Rietveld analysis.

Each sample was also prepared for a clay-size fraction (<2 μm) analysis. The samples were disaggregated and lightly crushed in a mortar mill. The disaggregated sample was transferred to a glass beaker and placed in an ultrasonic water bath to bring the clay into suspension. The solution containing suspended clay was centrifuged for 1 min at 1,100 rpm, transferred to a plastic beaker and placed in an oven at 60°C to dry down. The resulting clay floccules were powdered using a pestle and mortar; 45 mg was resuspended in 1.5-ml deionized water and pipetted onto glass slides. Each slide was analyzed air-dried and following an overnight ethylene glycol treatment (55°–60°C). Measurements were done between 2° and 50° 2θ (air-dried) or 2° and 20° 2θ (ethylene glycol) and a step-width of 0.02° 2θ. With the program EVA, the individual clay mineralogy and relative abundance was identified by their d-values, full width of half maximum (FWHM), and intensity.

Illite crystallinity was measured by quantifying the shape of the FWHM of dioctahedral illite-muscovite at the 10 Å spacing (Warr and Rice, 1994). The 10 Å peak measurement may include other phases in addition to illite (e.g., phengite and muscovite), which means illite crystallinity is a misleading term but one that is widely used in the literature (Merriman and Peacor, 1998). The presence of very fine grained micaceous mineral phases can compromise the interpretation of XRD peaks that overlap the illite reflection. The main uncertainty, however, is the presence of illite/smectite mixed layers, which result in asymmetrical broadening of the 10 Å peak. This effect disappears after ethylene glycol treatment, which allows for discrimination between the two minerals (Nieto et al., 1994; Battaglia et al., 2004).

The FWHM was determined graphically using the software package MacDiff 4.2.5 (http://www.ccp14.ac.uk/ccp/ccp14/ftp-mirror/krumm/Software/macintosh/macdiff/MacDiff.html), following a subtraction of background reflections, then converted to the Kübler scale (Warr and Rice, 1994), following the analysis of a set of interlaboratory standards (crystallinity index standards, CIS; Warr and Rice, 1994). The CIS are from the Variscan low-temperature metamorphic belt of North Cornwall and range from diagenetic to epizonal grades

(SW1, 2, 4, and 6). The average of three repeat measurements was plotted against CIS values and a correction factor determined via linear regression analysis. This calibration accounts for interlaboratory discrepancies that may arise due to sample preparation and data processing.

Results

Lithogeochemistry and principal component analysis

A correlation matrix for the entire PCA dataset (n = 2,705; sampling protocols 1 and 2) highlights some important correlations between the major elements (Table 1; the compositional data for the samples from protocol 2 are presented in Magnall et al., 2021). The strong correlation between Ca and Mg (r^2 = 0.97) means the bulk-rock concentration (mol/kg) of dolomite ($CaMg[CO_3]_2$) can be calculated on the basis of stoichiometry. Similarly, the concentrations (mol/kg) of the main sulfide minerals (pyrite, sphalerite, and galena) can be calculated from total S (i.e., $FeS_2 = 0.5 * $ (total S – [Pb + Zn]) and ZnS or PbS = total S – [2 * FeS_2]). The calculation of these sulfide mineral concentrations assumed that no other sulfide phases are present, which is confirmed by petrography and XRD results (see following sections). In Figure 5, downhole plots of sphalerite, pyrite, and dolomite concentration have been compared with gamma logs in TNDD015, TNDD012, and TNDD019. The B1 maximum flooding surface in the Teena subbasin corresponds with the peak gamma response and an interval (≤50 m) of highly abundant pyrite toward the base of the Middle HYC unit (B_1; Fig. 5). The Zn mineralized zone is located in the Lower HYC unit, 50 to 200 m beneath the B1 MFS.

The PCA shows that most (87%) of the total variance is described by three principal components (Fig. 6A). The scaled coordinates for individual elements show three principal groups that correspond with the siliciclastic (Al, K, Ti, P, Si) and sulfide (S, Fe, Pb and Zn) end members in PC1, and dolomite (Ca, Mg, Mn) in PC2 (Fig. 6B). The metals from the main sulfide phases (Fe, Pb, and Zn) are separated by PC3 (Fig. 6B). The composition of the different lithologic units can be visualized in a projection of scaled coordinates for each individual sample (Fig. 6C, D), which shows the relative contribution of each of the three end members. Samples from the Lower HYC unit (host unit of Lower and Main lenses Zn-Pb sulfide mineralization) occupy broadly similar PC1 to PC2 space as samples from the overlying Middle HYC unit (Fig. 6C). The trend toward negative PC1 and PC2 values represents increasing dolomite relative to the siliciclastic end member and is best preserved by samples from the W-Fold Shale Member and a number of samples from the Lower HYC unit (Fig. 6C). In terms of PC3, there is a small but important difference in where samples are grouped from the Lower and Middle HYC units (Fig. 6D), which represents the dominant sulfide mineral phases that are present (pyrite vs. sphalerite + galena).

There is a positive correlation between Ti and K in all units (r^2 = 0.72), although there is a subgroup of high K samples that are primarily from volcaniclastic sandstone beds in the Lower HYC unit in TNDD019 (Fig. 6E). There is a similar trend for Al and K covariation throughout all units, which overlaps a phengite end-member composition, apart from the

Table 1. A Correlation Matrix for the 2,705 Samples Used in the Principal Component Analysis

	Al	Ca	Fe	K	Mn	Pb	P	S	Si	Ti	Zn	Mg
Al	■	-0.37	-0.46	**0.81**	-0.39	-0.22	0.36	-0.35	**0.71**	**0.94**	-0.35	-0.21
Ca	-0.37	■	-0.09	-0.42	**0.94**	-0.54	0.03	-0.39	-0.13	-0.35	-0.53	**0.97**
Fe	-0.46	-0.09	■	-0.55	0.02	0.11	-0.59	**0.85**	**-0.77**	-0.35	0.28	-0.17
K	**0.81**	-0.42	-0.55	■	-0.48	0.01	0.44	-0.33	0.65	**0.72**	-0.11	-0.31
Mn	-0.39	**0.94**	0.02	-0.48	■	-0.45	-0.01	-0.30	-0.17	-0.36	-0.43	**0.88**
Pb	-0.22	-0.54	0.11	0.01	-0.45	■	-0.07	0.43	-0.28	-0.19	**0.90**	-0.64
P	0.36	0.03	-0.59	0.44	-0.01	-0.07	■	-0.62	**0.70**	0.29	-0.17	0.08
S	-0.35	-0.39	**0.85**	-0.33	-0.30	0.43	-0.62	■	**-0.75**	-0.23	0.57	-0.47
Si	**0.71**	-0.13	**-0.77**	0.65	-0.17	-0.28	**0.70**	**-0.75**	■	0.58	-0.42	-0.01
Ti	**0.94**	-0.35	-0.35	**0.72**	-0.36	-0.19	0.29	-0.23	0.58	■	-0.32	-0.20
Zn	-0.35	-0.53	0.28	-0.11	-0.43	**0.90**	-0.17	0.57	-0.42	-0.32	■	-0.64
Mg	-0.21	**0.97**	-0.17	-0.31	**0.88**	-0.64	0.08	-0.47	-0.01	-0.20	-0.64	■

group of high K samples that plot toward higher K/Al ratios and a more feldspathic composition (Fig. 6F).

Quantitative mineralogy (X-ray diffractometry; XRD)

The majority of samples selected for XRD analysis were from TNDD015 (n = 30) and TNDD019 (n = 27), which represents samples from very weakly and very strongly mineralized end members of the deposit (respectively) and includes all the major lithologic units of the Barney Creek Formation. The complete modal mineralogy of the 65 samples is presented in Table 2 and Figure 7. The dominant mineral phases in all units are quartz and dolomite, the latter of which is most abundant in the W-Fold Shale Member and Lower HYC unit. The main sulfide mineral is pyrite, which has the highest abundance in some samples from the Lower HYC unit (host to the stratiform sulfide mineralization) in TNDD019. In contrast, the abundance of pyrite within the Middle HYC unit is uniformly high in samples from all three drill holes. Feldspar is a major component of all units, predominantly orthoclase and microcline, with albite restricted to the more siliciclastic lithologies (Middle and Upper HYC units). Samples from the volcaniclastic sandstone beds contain particularly high concentrations of K-feldspar (orthoclase + microcline >20%).

Mass transfer analysis

The reference values used in the Gresens' analysis (Table 3) are provided by median compositions of the Lower HYC unit in TNDD015 (weakly mineralized) and moderate- to high-grade mineralization (>5% Zn) in the Main lens of TNDD019 (mineralized). These reference values represent compositional end members in the broader dataset, as represented by the PCA (Fig. 6C, D). The positive covariation between K (+Al), Si, and Ti, which is consistent in the subgroups of samples from TNDD015 (weakly mineralized) and TNDD019 (mineralized), is used as evidence for immobile element behavior. This is further supported by the clustering of these elements in the modified isocon plot (Fig. 8A). In the Gresens' plot

(Fig. 8B), there has been a major net gain in those elements associated with sulfide mineralization (Zn, Pb, Fe, As, Tl). Notably, this includes As and Tl concentrations that covary with pyrite and increase down sequence toward the Lower HYC unit (Fig. 8C, D). In terms of net element loss, this is entirely associated with dolomite (Ca, Mg, Mn, and Sr). There is no evidence, however, of any major bulk mass change in the altered samples, which would otherwise have produced an isocon with a slope that deviated substantially from 1.

The siliciclastic and dolomite end members, when represented by Ti and Ca, respectively, are negatively correlated (r^2 = 0.75) in the Lower HYC unit of TNDD015 (Fig. 8E). In TNDD012 and TNDD019, samples containing high concentrations of Zn plot away from this trend at low Ca concentrations (Fig. 8E). This means the linear regression between Ca (mol/kg) and Ti (mol/kg) in samples from TNDD015 (Fig. 8E, eq. 4) can be rearranged to calculate a value of calcium that might originally have been present in the mineralized samples (eq. 5):

$$Ti = -0.014 * Ca + 0.065 \tag{4}$$

and

$$Ca_{protolith} = (Ti - 0.065)/-0.014. \tag{5}$$

A value for calcium loss from mineralized samples can then be calculated from equation (6):

$$Ca_{loss} = Ca_{protolith} - Ca. \tag{6}$$

Values for Ca_{loss} have been calculated for the samples from the Main lens in TNDD019 and there is a good positive correlation (r^2 = 0.57) with Zn concentration (Fig. 8F). This positive correlation is weakened by the inclusion of the low Ti outliers that plot away from the detrital trend, which result in an apparent overestimation of Ca_{loss}. When the same calculation is applied to samples from TNDD012 there is no correlation between Ca_{loss} and Zn (Fig. 8F).
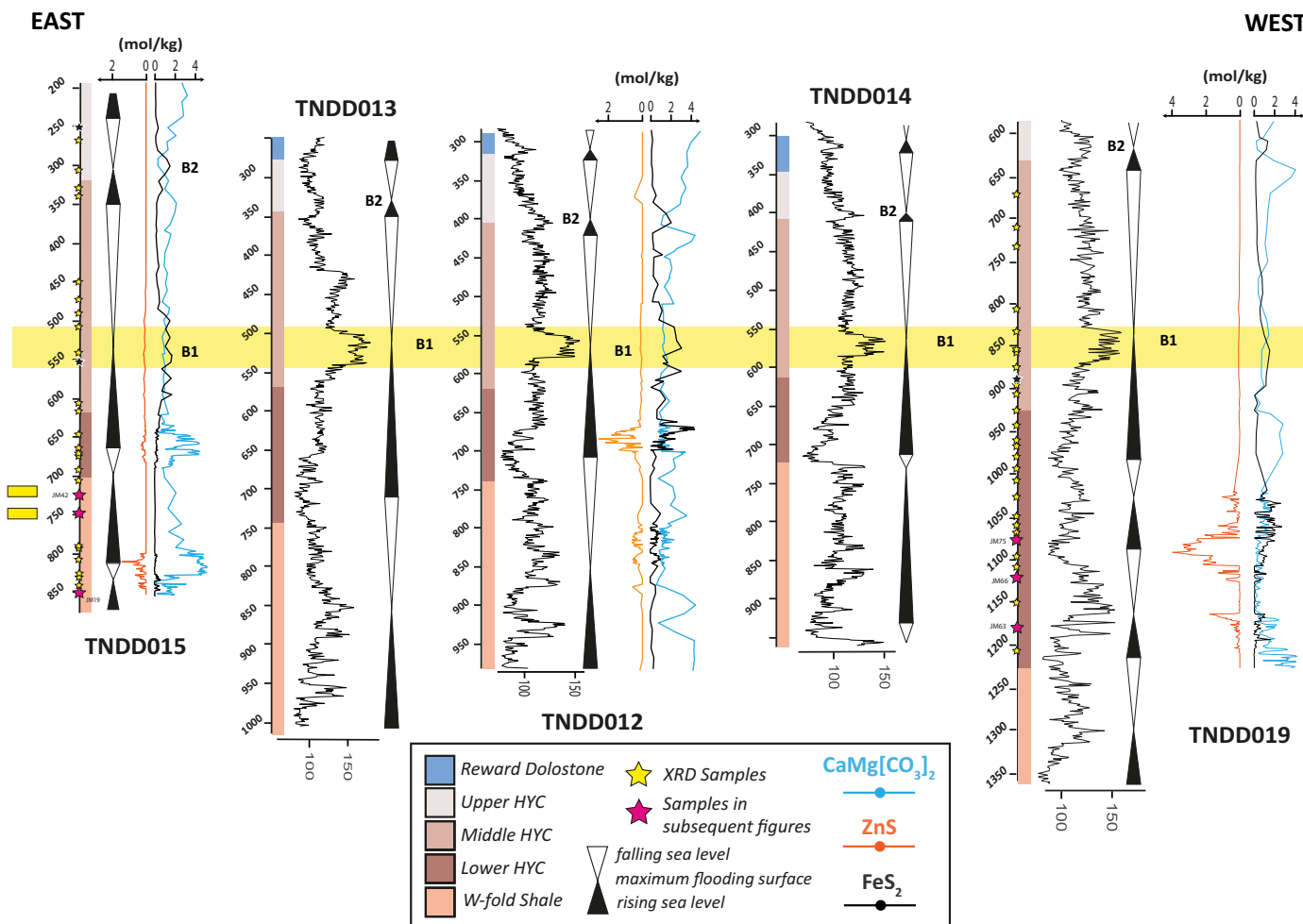
Fig. 5. Stratigraphic and downhole gamma logs and with calculated bulk-rock composition of key mineral phases (ZnS, FeS$_2$, and CaMg[CO3]$_2$). The gamma logs have been annotated to show 1st- and 2nd-order transgressive and regressive depositional cycles. The prominent peak in gamma response and pyrite abundance at the base of the Middle HYC unit (B1, yellow band) corresponds with a regional (1st-order) maximum flooding surface (MFS) that has been described in other subbasins in the Batten fault zone (Kunzmann et al., 2019). The yellow stars denote samples that were selected for X-ray diffractometry analysis and pink stars denote those that are described in more detail in subsequent figures.

Phyllosilicate mineralogy and illite crystallinity

The clay-size fraction results differentiate between illite, phengite, and muscovite and help to determine the presence of smectite and/or illite-smectite mixed layers that are otherwise not easily distinguishable from bulk powder analyses (as they have the same 001, 002, and 020 peak positions). Diffractograms for samples from the different lithologic units are shown in Figure 7. Illite can be distinguished from muscovite by the broad [001] reflection, which is identifiable in most lithologies but is most pronounced in samples from the Middle HYC unit. In contrast, the samples containing higher concentrations of dolomite (W-Fold Shale Member and Lower HYC unit) have a much less pronounced illite [001] peak. Chlorite is also present in most samples, as determined from the [002] peak. From the clay fraction analyses chlorite appears to be present primarily as the Fe-rich end member chamosite, which tends to lack a prominent first basal [001] reflection (Fig. 7).

In general, changes in illite crystallinity correspond with the relative proportions of the dolomite and siliciclastic end members in each sample. For example, the lowest full width half maximum values are in samples from the W-Fold Shale Member and Lower HYC unit (Fig. 9A). In contrast, the highest full width half maximum values are in samples from the Middle and Upper HYC units, together with samples from coarse-grained volcaniclastic beds. In several samples from the mineralized drill holes (TNDD012 and TNDD019) the full width half maximum of the [001] peak is lower in ethylene glycol treated samples (compared to air-dried), indicating the presence of some smectite interlayers. In contrast, samples from TNDD015 preserve no evidence of smectite content.

Organic maturity

The concentration of total organic carbon (TOC) in the Lower, Middle, and Upper HYC units varies between 1.2 and 4.4 wt %. The highest TOC concentrations are at the MFS (>4%). In the small number of samples analyzed for thermal maturity the hydrogen index (HI; mg HC/g TOC) is between 7 and 44 (Fig. 9B), and hydrocarbon generative potential
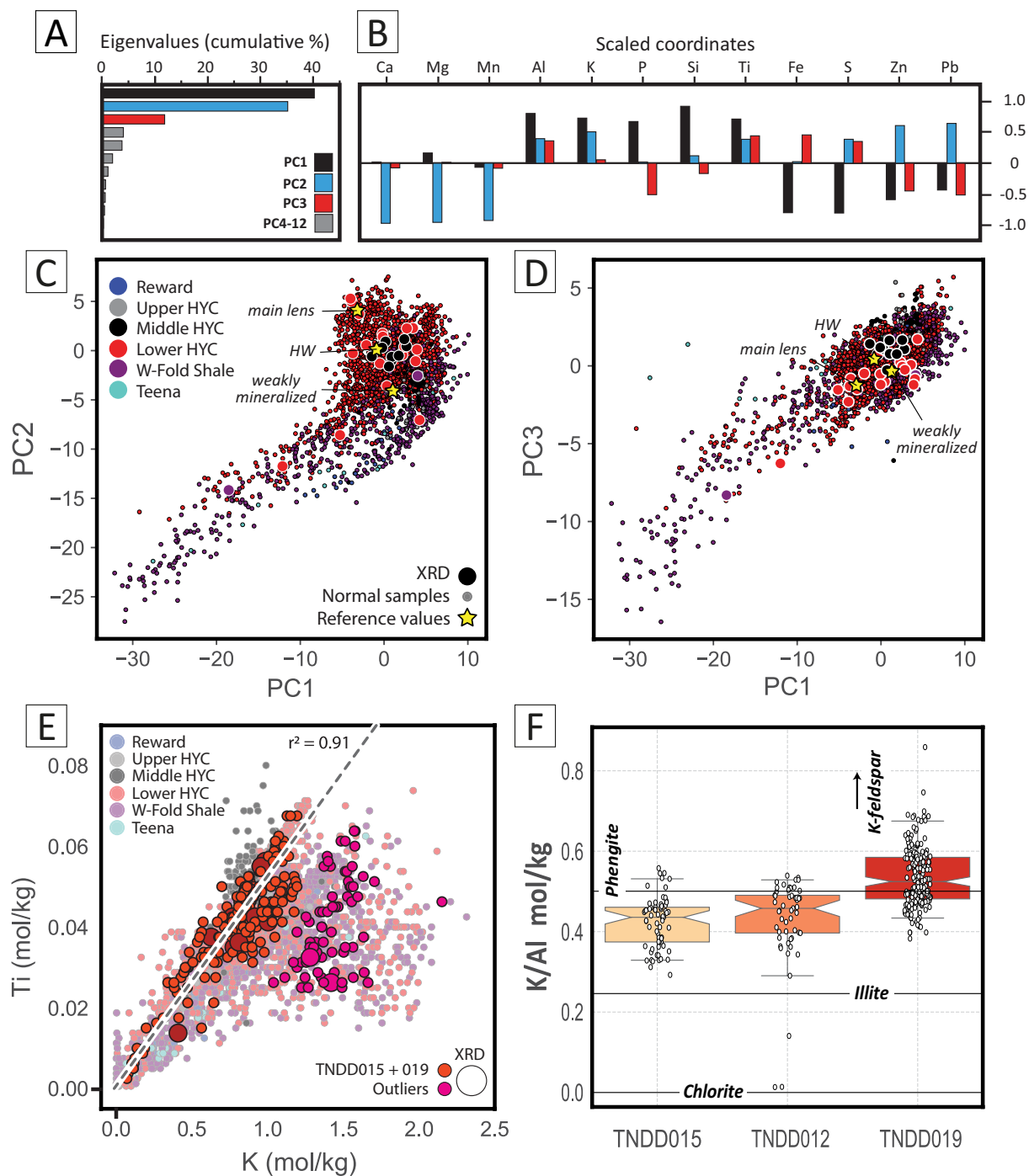
Fig. 6. Summary of the PCA conducted on the lithogeochemical data set ($n = 2,705$). (A). The total variance (%) described by each individual component of the principal component analysis (PCA). The first three principal components describe 87% of the total variance in the dataset. (B). Eigenvector coefficients for each element in the first three principal components. Positive values in PC1 describe the sulfide mineralogy (Fe, Pb, Zn, and S), whereas PC2 discriminates between shale (Al, K, Ti, P, Si) and carbonate (Ca, Mg, Mn). Pyrite, sphalerite, and galena are separated by PC3. (C). A bivariate plot of the scaled coordinates for the PC1 and PC2 of each individual sample. The samples chosen for XRD analysis are represented by enlarged symbols. Reference values used in the subsequent Gresens' analysis (Fig. 7) are shown as stars. (D). A bivariate plot of the scaled coordinates for the PC1 and PC3 of each individual sample. The symbols are the same as in (C). (E). A plot of K vs. Ti (mol/kg) for all samples, in which those samples from TNDD015 and TNDD019 are emphasized. Most samples plot along the trend line for TNDD015 and the subgroup of outliers is associated with samples containing volcani-clastic sandstone beds. (F). Box and whisker plots for bulk-rock K/Al ratios in samples from the Lower HYC unit in the three drill holes (TNDD015, TNDD012, and TNDD019). The notch in the box corresponds with the median value and the box extends to the 25th and 75th percentiles (tails extend to the 5th and 95th percentiles). Horizontal lines represent K/Al ratios of the labeled mineral phases.
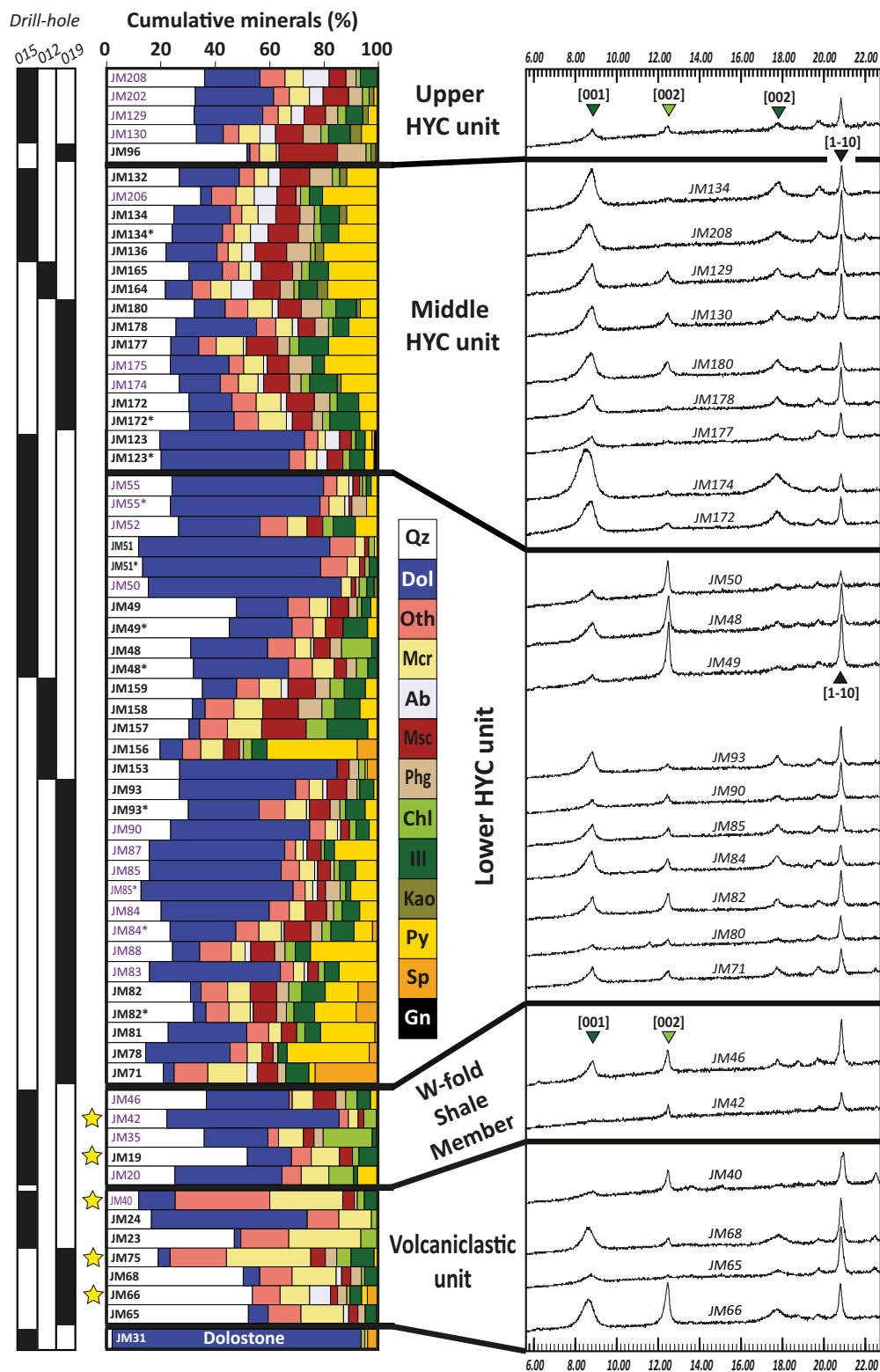
Fig. 7. The modal mineralogy of individual samples determined from quantitative X-ray diffractometry (XRF) analysis normalized to 100%. Drill hole information is denoted by the black bars on the left-hand side and samples are ordered by stratigraphic units. Sample names in purple correspond with petrographic samples that have no corresponding bulk-rock lithogeochemical data (and so are excluded from the principal component analysis). Yellow stars correspond with samples that are shown in subsequent petrographic figures. The X-ray diffractograms for the clay fraction (<2 μm, air-dried) are shown on the right-hand side with the reflections of the main mineral phases annotated with colored triangles. Ab = albite, Chl = chlorite, Dol = dolomite, Gn = galena, Ill = illite, Kao = kaolinite, Mcr = microcline, Msc = muscovite, Oth = orthoclase, Phg = phlogopite, Py = pyrite, Qz = quartz, Sp = sphalerite.

Table 2. Quantitative XRD and Illite Crystallinity Data for Samples from the Different Lithologic Units in the Teena Subbasin
Major Mineral Phases (>1%).

Drill hole	Unit	Depth (m)	Sample	Mineral (%)							
				Qz	Dol	Ab	Kao	Phg	Chl	Oth	Mcr
TNDD015	Middle HYC	269.8	JM208	36.0	20.4	9.5	<1	3.7	1.6	9.2	6.7
TNDD015	Middle HYC	337	JM202	32.6	28.8	5.0	1.8	5.1	2.4	5.8	7.4
TNDD015	Middle HYC	450.7	JM129	32.2	25.2	4.7	2.0	4.5	3.0	5.7	4.8
TNDD015	Middle HYC	474.9	JM130	33.0	9.9	5.7	4.1	6.5	2.8	5.7	7.8
TNDD019	Middle HYC	906.9	JM96	51.6	1.1	1.0	1.8	10.5	1.8	3.5	6.2
TNDD015	Middle HYC (mfs)	489.9	JM132	26.7	22.1	4.3	2.6	8.3	2.7	5.5	5.2
TNDD015	Middle HYC (mfs)	300.6	JM206	34.6	4.0	8.3	<1	1.7	3.3	9.0	6.7
TNDD015	Middle HYC (mfs)	508.6	JM134	24.7	20.8	6.5	2.7	5.3	2.2	4.2	6.0
TNDD015	Middle HYC (mfs)	508.6	JM134*	24.1	18.5	6.5	<1	5.7	2.8	4.3	6.0
TNDD015	Middle HYC (mfs)	541.5	JM136	21.8	18.8	4.8	3.1	8.8	1.7	4.1	5.0
TNDD012	Middle HYC (mfs)	541.9	JM165	30.2	12.4	3.9	<1	3.3	2.8	6.0	4.4
TNDD012	Middle HYC (mfs)	550.9	JM164	21.6	9.9	8.2	3.8	5.1	1.9	6.8	7.5
TNDD019	Middle HYC (mfs)	805.4	JM180	32.2	11.4	2.2	1.4	7.5	5.2	8.3	9.0
TNDD019	Middle HYC (mfs)	836.5	JM178	25.5	29.6	2.1	<1	5.0	1.6	7.1	6.1
TNDD019	Middle HYC (mfs)	854.5	JM177	23.6	10.3	1.1	<1	4.4	3.4	6.4	10.0
TNDD019	Middle HYC (mfs)	857.4	JM175	23.4	21.6	1.3	<1	8.6	<1	5.4	7.3
TNDD019	Middle HYC (mfs)	872.7	JM174	26.7	15.1	2.0	1.4	4.2	3.2	6.7	7.2
TNDD019	Middle HYC (mfs)	895.5	JM172	30.3	15.8	2.0	<1	5.7	2.7	8.9	9.1
TNDD019	Middle HYC (mfs)	895.5	JM172	30.5	16.4	2.2	<1	3.8	2.7	8.9	10.3
TNDD015	Lower HYC	602.6	JM123	19.9	53.3	5.3	<1	<1	1.6	4.9	2.7
TNDD015	Lower HYC	602.6	JM123	20.4	47.2	3.8	<1	<1	2.5	5.9	4.2
TNDD015	Lower HYC	616.4	JM55	24.4	55.8	1.5	<1	1.0	1.4	4.9	4.4
TNDD015	Lower HYC	616.4	JM55	23.8	55.1	1.5	<1	5.4	<1	3.3	5.8
TNDD015	Lower HYC	646.1	JM52	26.8	30.0	<1	<1	<1	3.8	10.1	7.2
TNDD015	Lower HYC	665.7	JM51	12.1	70.4	<1	<1	<1	2.1	9.3	3.5
TNDD015	Lower HYC	665.7	JM51	13.6	65.5	<1	<1	<1	1.6	9.8	4.5
TNDD015	Lower HYC	668.2	JM50	15.7	71.0	<1	1.2	1.3	2.8	<1	3.7
TNDD015	Lower HYC	673.6	JM49	48.1	19.0	1.1	<1	3.2	1.6	7.9	6.7
TNDD015	Lower HYC	673.6	JM49	45.5	23.1	<1	<1	<1	<1	7.7	4.6
TNDD015	Lower HYC	681.3	JM48	31.3	28.3	1.0	<1	4.2	11.1	10.1	5.8
TNDD015	Lower HYC	681.3	JM48	32.3	35.0	<1	<1	3.7	4.2	8.8	8.0
TNDD012	Lower HYC	624.6	JM159	35.6	12.6	2.5	<1	5.4	5.2	8.3	8.1
TNDD012	Lower HYC	649.4	JM158	31.9	4.7	<1	<1	8.7	4.7	10.6	10.6
TNDD012	Lower HYC	661.3	JM157	30.6	4.0	<1	<1	<1	7.7	10.2	12.6
TNDD012	Lower HYC	671.4	JM156	20.0	8.3	<1	<1	1.5	3.1	6.7	8.4
TNDD012	Lower HYC	701.6	JM153	27.2	58.0	<1	<1	3.5	2.4	<1	<1
TNDD019	Lower HYC	961.6	JM88	24.6	10.0	2.1	<1	3.8	3.8	11.6	5.1
TNDD019	Lower HYC	1,011	JM83	16.1	48.2	1.3	<1	<1	2.2	4.8	4.0
TNDD019	Lower HYC	1,029	JM82	31.2	3.9	<1	<1	4.5	4.8	9.8	8.3
TNDD019	Lower HYC	1,028.6	JM82	32.3	4.6	1.1	<1	3.6	2.8	8.5	7.8
TNDD019	Lower HYC	1,048	JM81	23.0	28.9	<1	<1	<1	3.0	8.1	4.7
TNDD019	Lower HYC	1,069	JM78	14.7	31.1	<1	<1	1.8	<1	6.3	5.4
TNDD019	Lower HYC	1,094.3	JM71	21.2	4.0	3.8	<1	3.0	<1	12.4	14.4
TNDD019	Lower HYC	929	JM93	27.1	42.8	1.5	<1	3.8	1.0	5.0	5.0
TNDD019	Lower HYC	929	JM93	30.4	26.1	1.1	<1	3.6	2.1	9.5	7.9
TNDD019	Lower HYC	946.8	JM90	23.9	51.2	1.2	<1	<1	2.4	5.7	4.5
TNDD019	Lower HYC	968.2	JM87	16.0	49.9	1.4	<1	<1	1.2	4.0	2.8
TNDD019	Lower HYC	977.8	JM85	16.1	48.5	1.1	<1	1.4	2.0	6.7	5.6
TNDD019	Lower HYC	977.8	JM85	13.0	56.0	1.7	<1	5.4	2.1	4.4	2.8
TNDD019	Lower HYC	990.3	JM84	20.4	39.8	<1	<1	2.6	3.1	7.4	5.8
TNDD019	Lower HYC	990.3	JM84	23.7	24.2	1.0	<1	4.1	3.3	8.5	8.3
TNDD015	W-Fold Shale	709.95	JM46	37.1	30.5	<1	<1	3.6	4.2	1.2	7.8
TNDD015	W-Fold Shale	726.7	JM42	22.5	63.6	<1	<1	<1	4.6	3.4	3.6
TNDD015	W-Fold Shale	794	JM35	36.3	23.5	<1	<1	3.4	18.1	3.9	9.2
TNDD015	W-Fold Shale	850.8	JM19	52.2	16.3	<1	<1	<1	2.4	7.3	10.4
TNDD015	W-Fold Shale	884.8	JM20	25.4	39.6	<1	<1	<1	9.1	7.1	10.2
TNDD015	Mass flow	749.6	JM40	12.1	13.3	<1	<1	1.1	2.6	34.9	26.9
TNDD015	Mass flow	832	JM24	16.8	57.5	<1	<1	<1	2.0	11.7	12.0
TNDD019	Mass flow	1,076	JM75	19.3	4.4	<1	<1	4.2	5.3	20.8	31.1
TNDD019	Mass flow	1,112.4	JM68	50.7	6.1	2.0	<1	3.9	1.2	11.9	16.3
TNDD019	Mass flow	1,124.9	JM66	54.1	<1	7.7	<1	3.4	1.2	10.2	10.9
TNDD019	Mass flow	1,150.8	JM65	52.6	7.3	1.9	<1	2.7	<1	12.1	15.7
TNDD015	Mass flow	835.8	JM23	47.4	2.4	<1	<1	<1	5.9	17.7	26.6
TNDD015	Dolostone	808.3	JM31	2.3	91.9	<1	<1	<1	1.4	<1	<1

Notes: Quantitative mineralogy is given in % and has been normalized to 100%; the 10 Å peak measurement has been converted to the Kübler scale (10 Å °);
mfs = maximum flooding surface, XRD = X-ray diffractometry; Ab = albite, Chl = chlorite, Dol = dolomite, Kao = kaolinite, Mcr = microcline, Oth = ortho-
clase, Phg = phlogopite, Qtz= quartz.

Table 2. (*Cont.*)

Drill hole	Mineral (%)					Air dried				Ethylene glycol			
	Py	Ill	Msc	Sp	Gn	10A	d [Å]	I [C]	10A °	10A	d [Å]	I [C]	10A °
TNDD015	<1	6.7	6.2	<1	<1	0.68	10.17	1,105	0.99	0.60	10.11	843	0.87
TNDD015	1.6	<1	9.4	<1	<1								
TNDD015	3.7	6.2	7.9	<1	<1								
TNDD015	6.4	8.0	10.2	<1	<1								
TNDD019	1.0	<1	21.5	<1	<1								
TNDD015	11.6	<1	10.9	<1	<1								
TNDD015	20.6	4.8	7.0	<1	<1	0.42	10.05	426	0.61				
TNDD015	11.8	7.0	8.9	<1	<1	0.34	10.03	583	0.49	0.34	10.00	556	0.49
TNDD015	14.4	6.4	11.1	<1	<1	0.55	10.05	1,614	0.80				
TNDD015	20.3	<1	11.7	<1	<1								
TNDD012	18.3	7.1	11.5	<1	<1	0.35	10.00	509	0.51	0.31	9.97	466	0.44
TNDD012	18.7	6.7	9.8	<1	<1	0.45	10.03	510	0.65	0.42	9.96	511	0.61
TNDD019	6.8	7.6	8.5	<1	<1	0.60	10.12	1,429	0.87	0.44	10.02	1,323	0.64
TNDD019	10.9	5.9	6.2	<1	<1	0.48	9.99	1,060	0.69	0.38	10.02	1,000	0.54
TNDD019	18.4	10.9	11.5	<1	<1	0.44	10.02	628	0.63	0.47	10.03	547	0.68
TNDD019	19.8	4.5	8.0	<1	<1	0.49	10.00	1,405	0.71	0.50	10.00	1,405	0.73
TNDD019	13.7	10.1	9.6	<1	<1	0.80	10.31	2,515	1.16	0.71	10.06	1,761	1.03
TNDD019	7.2	7.9	10.3	<1	<1	0.60	10.12	1,633	0.87	0.60	10.12	1,633	0.87
TNDD019	6.7	11.0	7.3	<1	<1								
TNDD015	2.5	3.5	4.3	1.0	1.0								
TNDD015	3.5	5.5	5.8	<1	1.1	0.28	10.02	538	0.41	0.33	9.99	433	0.47
TNDD015	2.2	1.8	2.5	<1	<1	*0.28*	*10.00*	*116*	0.41				
TNDD015	4.0	<1	1.1	<1	<1								
TNDD015	8.1	8.2	5.8	<1	<1								
TNDD015	1.1	<1	1.5	<1	<1								
TNDD015	<1	2.9	2.0	<1	<1								
TNDD015	<1	2.7	1.6	<1	<1	*0.30*	*10.05*	*474*	0.44				
TNDD015	2.3	3.4	6.6	<1	<1								
TNDD015	3.6	9.0	6.5	<1	<1	*0.25*	*10.00*	*386*	0.35	*0.24*	*9.97*	*365*	0.35
TNDD015	<1	2.2	6.1	<1	<1								
TNDD015	<1	3.4	4.5	<1	<1	0.47	10.03	760	0.68	0.48	10.02	657	0.69
TNDD012	4.4	7.8	10.1	<1	<1	0.67	10.03	5,534	0.98	0.46	10.02	1,499	0.66
TNDD012	6.4	9.3	13.1	<1	<1								
TNDD012	3.6	15.0	16.4	<1	<1								
TNDD012	33.2	5.6	5.8	7.5	<1								
TNDD012	0.8	<1	4.4	3.6	<1								
TNDD019	24.4	5.6	8.8	<1	<1	0.39	10.00	521	0.56	0.25	9.97	607	0.36
TNDD019	14.1	5.4	3.9	<1	<1	0.33	10.02	192	0.48	0.19	10.08	197	0.27
TNDD019	12.1	8.6	9.7	7.2	<1	0.35	9.99	1,051	0.51	0.34	10.00	1,029	0.49
TNDD019	15.3	7.6	8.6	7.8	<1								
TNDD019	20.0	5.8	5.6	1.0	<1								
TNDD019	30.2	3.4	4.1	<1	<1	0.34	10.03	945	0.49	0.30	10.03	236	0.43
TNDD019	2.3	8.5	7.5	23.0	<1	0.31	10.00	899	0.45	0.26	10.00	912	0.37
TNDD019	1.4	5.2	7.3	<1	<1								
TNDD019	4.4	7.2	7.6	<1	<1	0.40	10.00	1,221	0.58	0.36	10.00	1,105	0.52
TNDD019	3.0	4.9	3.2	<1	<1	0.31	10.08	460	0.44	0.32	9.99	462	0.46
TNDD019	16.0	3.7	5.2	<1	<1	0.47	10.08	193	0.68	0.21	9.99	262	0.29
TNDD019	7.8	5.9	4.7	<1	<1								
TNDD019	9.8	1.8	3.0	<1	<1	0.40	10.02	969	0.58	0.30	10.00	953	0.43
TNDD019	6.5	6.5	7.9	<1	<1	0.46	10.03	1,313	0.67	0.42	10.02	1,244	0.60
TNDD019	6.8	8.5	9.8	2.0	<1								
TNDD015	2.3	5.0	8.3	<1	<1	0.38	10.02	793	0.55	0.32	10.01	761	0.46
TNDD015	<1	<1	2.1	<1	<1								
TNDD015	<1	1.6	3.9	<1	<1								
TNDD015	<1	6.7	4.8	<1	<1	0.37	9.97	301	0.54	0.37	10.00	311	0.53
TNDD015	7.1	1.5	<1	<1	<1	*0.10*	*10.10*	*118*	*0.14*	*0.10*	*10.40*	*519*	*0.14*
TNDD015	<1	4.6	4.3	<1	<1	0.52	10.00	251	0.76				
TNDD015	<1	<1	<1	<1	<1								
TNDD019	1.1	8.5	5.4	<1	<1	0.61	10.18	9,019	0.88	0.58	10.00	2,035	0.84
TNDD019	<1	4.6	3.4	<1	<1	0.58	10.28	1,234	0.84	0.66	9.92	909	0.96
TNDD019	2.1	4.3	2.6	3.6	<1	0.58	10.26	1,572	0.85	0.61	10.00	1,288	0.88
TNDD019	<1	4.2	3.4	<1	<1	0.47	10.09	477	0.68	0.56	9.97	419	0.81
TNDD015	<1	<1	<1	<1	<1	*0.20*	*10.00*	*132*	*0.28*	*0.20*	*10.00*	132	0.28
TNDD015	1.0	<1	<1	3.4	<1								

Table 3. Reference Compositions Used for the Chemical
Mass-Balance Analysis

	TNDD015	Main Lens[1]	Hanging wall[2]
n	65	32	62
SiO_2 (%)	43.8	33.9	42.6
Al_2O_3 (%)	8.3	8.2	9.6
Fe (%)	4.5	7.5	10.2
MgO (%)	7.6	1.8	3.9
CaO (%)	10.0	1.9	4.6
K_2O (%)	3.0	4.4	4.2
TiO_2 (%)	0.270	0.340	0.340
P (%)	0.072	0.076	0.080
MnO (%)	0.440	0.060	0.200
Ba (%)	0.033	0.027	0.028
Co (%)	0.002	0.003	0.003
Sr (%)	0.010	0.002	0.003
V (%)	0.003	0.013	0.014
Zr (%)	0.010	0.024	0.014
S (%)	1.9	15.4	10.7
Cu (%)	0.003	0.007	0.012
Pb (%)	0.025	2.605	0.242
Zn (%)	0.4	16.7	1.6
Ni (%)	0.003	0.004	0.006
As (ppm)	138.0	2110.0	631.0
Cd (ppm)	4.7	170.5	11.5
Sb (ppm)	5.0	17.4	17.0
Ag (ppm)	0.2	0.8	0.7
Tl (ppm)	13.6	211.0	126.0
Ge (ppm)	4.0	40.4	10.3

Notes: The compositions are median values calculated for samples that have
been screened for low Ti outliers
[1] 1,072 to 1,107 m in TNDD019
[2] 1,020 to 1,072 m in TNDD019

(S2; mg HC/g TOC) is low (0.09–0.91). The organic matter is classified as Type IV (inert). Further results are presented in Table 4.

Hyperspectral imaging

The hyperspectral imaging provides information about the core box scale distribution of phyllosilicate and carbonate phases within individual stratigraphic units (e.g., Fig. 10). There is a strong lithologic control on the phyllosilicate mineralogy, whereby the more carbonaceous beds contain phengite and the finer grained claystone beds, located at the top of graded volcaniclastic sandstone beds, contain pervasive illite-muscovite alteration (Fig. 10D). The chlorite adjacent to nodules in the W-Fold Shale Member is Fe rich, whereas chlorite in the mudstone laminae is more Mg rich (Fig. 10G). The nodules that are peripherally altered by Fe-rich chlorite preserve evidence of compositional zonation with high Ca dolomite at their margins. This relationship is much weaker or nonexistent in dolomite nodules in Lower HYC unit.

Petrography and paragenesis

The following section describes the paragenetic relationships from representative samples from the W-Fold Shale Member and Lower HYC unit. The descriptions primarily focus on the major mineral phases (as determined by XRD) and are organized in terms of paragenesis.

Fine-grained pyrite, dolomite, and hematite are the three main phases in the first stage of the paragenesis. Fine-grained aggregates of microeuhedral pyrite (py1a) are characteristic of most lithologies in the Lower and Middle HYC units and are also abundant in carbonaceous intervals in the middle W-Fold Shale Member. Individual pyrite crystals are very small (<5 μm) and are disseminated in layers between detrital K-feldspar and quartz grains and amorphous organic matter (Fig. 11A, B). A second generation of larger euhedral pyrite (py1b) is found both in and on the outer margins of dolomite nodules (Fig. 11C).

There are two types of early dolomite in the W-Fold Shale Member and Lower HYC unit: (1) fine-grained dolomite cement, and (2) mesoscopic nodules. The nodules have a range of morphologies, including (1) large ovoid (>5-cm-diam) nodules in nonpyritic, carbonaceous siltstone and mudstone; (2) small (<0.5-cm) spherical nodules with radial fibrous texture in pyritic, carbonaceous mudstone in the Lower HYC unit and middle W-Fold Shale Member; (3) elongate tabular nodules that locally overprint smaller nodules (both units) and commonly extend beyond the diameter of the drill core; (4) irregular lensoidal nodules (1–5 cm) in dolomitic siltstone and mudstone (W-Fold Shale Member); and (5) wormy dolomite veinlets and blebs (cf. molar tooth structure) found exclusively in the volcaniclastic sandstone beds.

Microinclusions of hematite in early generations of dolomite impart a pale-red dusty coloration that is characteristic of dolomite nodules and beds in the W-Fold Shale Member (Fig. 12). They are identified by the bright response in the backscatter electron images (enclosed within the red dashed outline for dolomite; Fig. 12G). Hematite is broadly distributed through lower and upper parts of the unit, as well as in upper part (1–50 m) of the Teena Dolostone (Fig. 3C). It is most strongly developed toward the southern margin of the subbasin, where it overprints both dolomite nodule and siltstone beds. Alternating layers of red (hematite-bearing) nodular dolostone and green siltstone are common throughout the W-Fold Shale Member in other subbasins throughout the

Fig. 8. (A). A modified isocon diagram in which the sum of the square for each analyte is equal to 1. The colors correspond with the three main principal components and the enlarged symbols represent immobile elements associated with the siliciclastic end member. (B). An isocon diagram in which a median composition of 65 samples from the Lower HYC unit from TNDD015 (weakly mineralized) has been compared to the median composition of 32 samples from the Lower HYC unit in TNDD019. Any outlier samples from the primary detrital trend (Fig. 6E) have been excluded. The dashed line represents the isocon, along which there is zero net change. (C). Pyrite (mol/kg) vs. As (ppm) for the Upper, Middle, and Lower HYC units. (D). Pyrite (mol/kg) vs. Tl (ppm) for the Upper, Middle, and Lower HYC units. (E). Ca vs. Ti (mol/kg) in samples from the Lower (red) and Middle (black) HYC unit for samples from TNDD015 and TNDD019. (F). Ca_{loss} vs. Zn (mol/kg) in samples from the Lower HYC unit in TNDD019 (red) and TNDD012 (purple). The solid trend line shows the molar volume ratio (1:2.7) of the reaction involving sphalerite (23.83 cm³) replacement of dolomite (64.35 cm³). The narrow diamond symbol corresponds with those samples that are from outside the Main lens but still preserve Zn grades >5%. The triangles represent the outliers from the primary detrital trend.
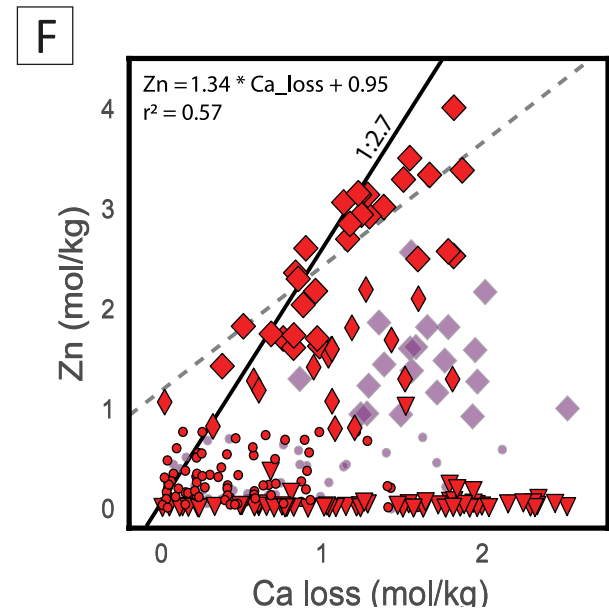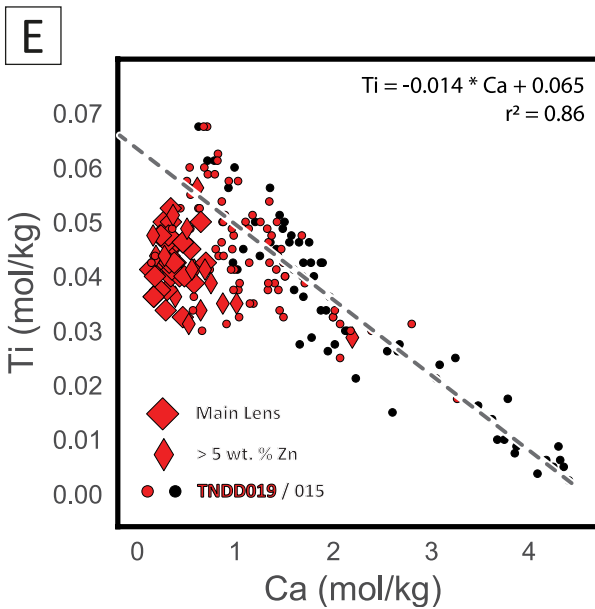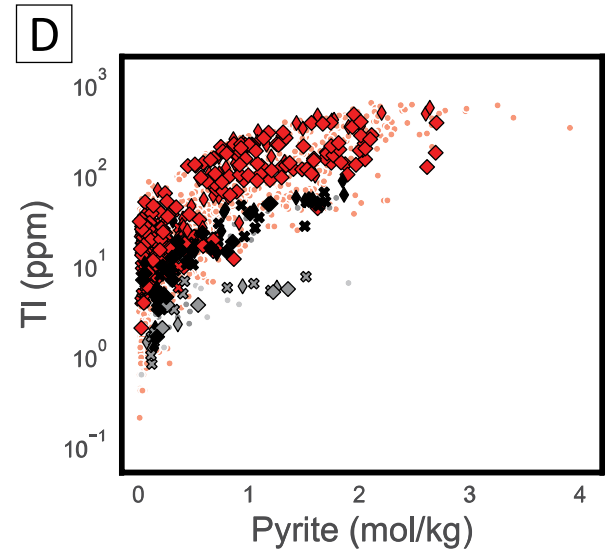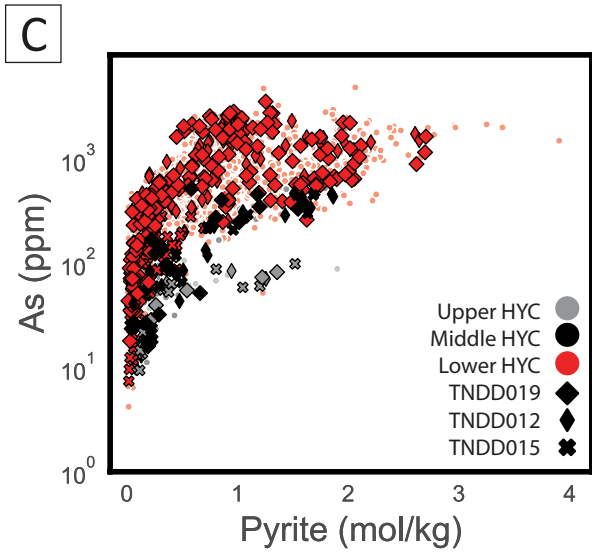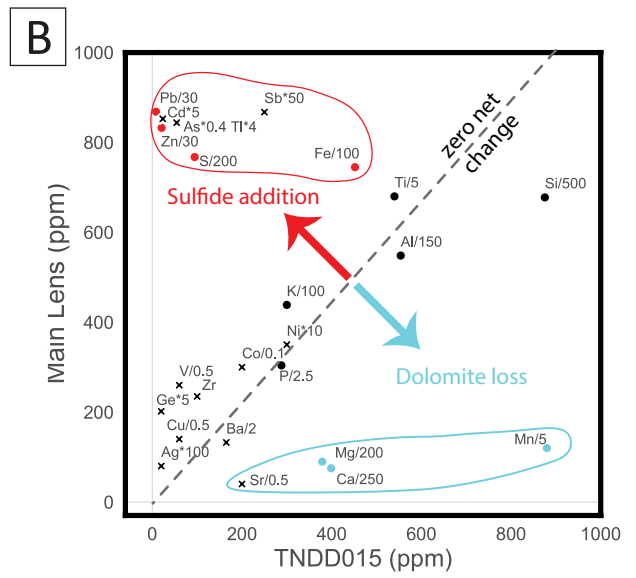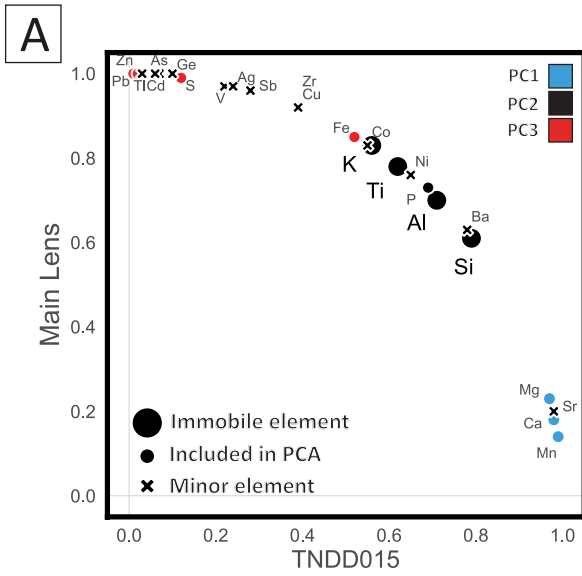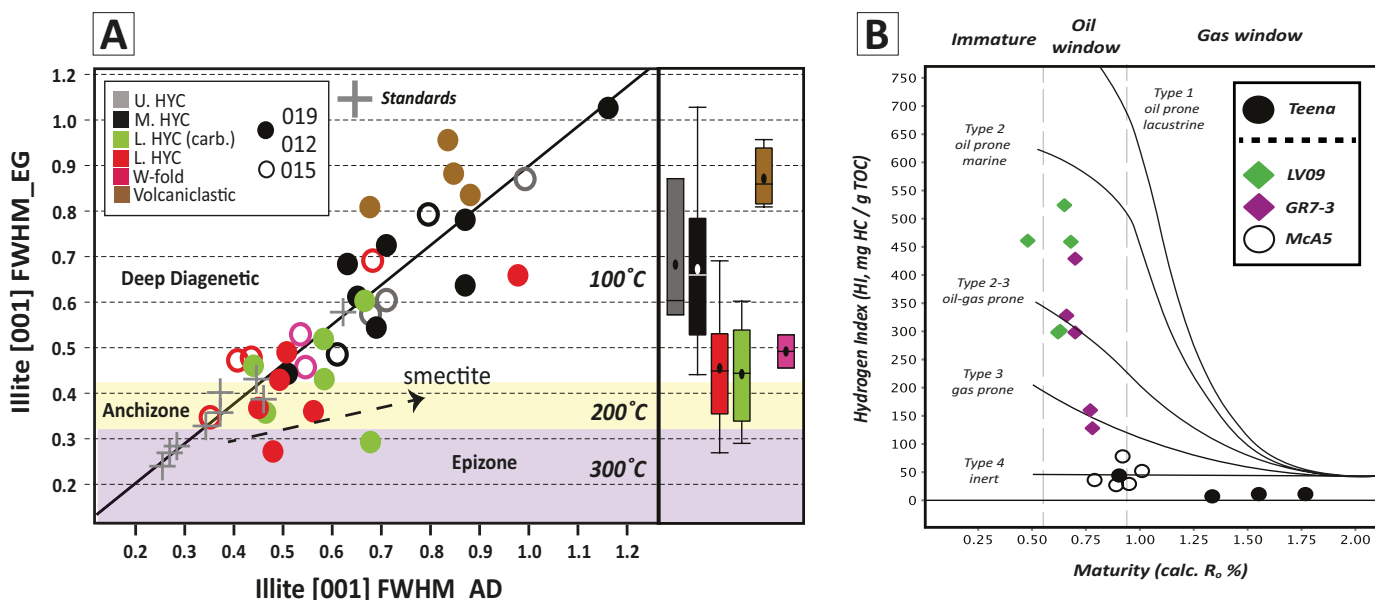
Fig. 9. (A), The full width half maximum (FWHM) of the [001] illite peak from air-dried (AD) and ethylene glycol (EG) analyses of the clay fraction ($<2\,\mu$m). Samples from the Lower HYC unit with abundant dolomite (>30%) have been grouped separately as L. HYC (carb.). Linear regression is through the standards (gray crosses), with r^2 = 0.95 (y = 0.86 * x + 0.04). Samples from TNDD015 follow a similar regression as the standards, whereas samples from TNDD012 and TNDD019 have a shallower slope due to presence of smectite. The boxplot is shown for EG analyses on the right, where tails extend from 5th to 95th percentile, and lines and circles correspond with median and average values, respectively. (B). Modified van Krevelen diagram showing the type and nature of organic matter with maturity (calculated as R_o%; see methods) plotted against hydrogen index (HI, mg HC/g total organic carbon (TOC)). Also included are data from regional drill holes within the McArthur Basin (black, green, and purple symbols; data from Baruch et al., 2015).

McArthur Basin and are not directly spatially associated with mineralization (Hayward et al., 2021).

Potassium feldspar and quartz: There is abundant potassium feldspar and quartz, particularly in coarser-grained siliciclastic intervals of the W-Fold Shale Member and the volcaniclastic sandstone beds. The most accurate Rietveld refinements are produced with the inclusion of both microcline and orthoclase from the database, which is consistent with petrographic evidence that shows two K-feldspar phases in an assemblage with quartz (e.g., Fig. 12F). The K-feldspar and quartz assemblage also forms a patchy microcrystalline replacement of some dolomite nodules within the W-Fold Shale Member (e.g., Fig. 12F), and a microcrystalline cement to coarse-grained volcaniclastic sandstone beds (e.g., Fig. 13).

Chlorite, illite, and phengite: There is a strong lithostratigraphic control on the distribution of chlorite, illite, and phengite. The finer grained, more carbonaceous intervals contain an approximately uniform distribution of phengite, although there is evidence of some compositional variability that is concentrated in texturally destructive metasomatic alteration

zones that are volumetrically minor (Fig. 10B). Chlorite is concentrated on the margins of dolomite nodules in the W-Fold Shale Member, whereas the matrix of some fault breccias and volcaniclastic sandstone beds have undergone intense illitization (e.g., Fig. 10D). The chlorite associated with dolomite has distinctive, bladed, pore-filling crystals (Fig. 14F), which EDS analyses show is Fe bearing (consistent with XRD analyses). Hyperspectral imaging shows that there is also an Mg-rich chlorite end member that is confined to the mudstone laminations. In the HYC units in which illite and phengite are most abundant, they form a fine-grained amorphous cement in the pore spaces between detrital clasts (Fig. 15). Illite and phengite cementation does not completely occlude porosity, however, and there are small micrometer cavities preserved within the cement (Fig. 15D).

Hydrothermal pyrite, galena, and sphalerite: Hydrothermal mineralization was associated with the formation of large, subhedral to rounded, crystals of pyrite (py2) and an assemblage of fine-grained sphalerite (sp1) with subordinate amounts of galena (gn1). The pyrite is commonly porous and forms strat-

Table 4. Thermal Maturity Indicators for a Small Number of Organic-Rich Samples from the Middle HYC Unit

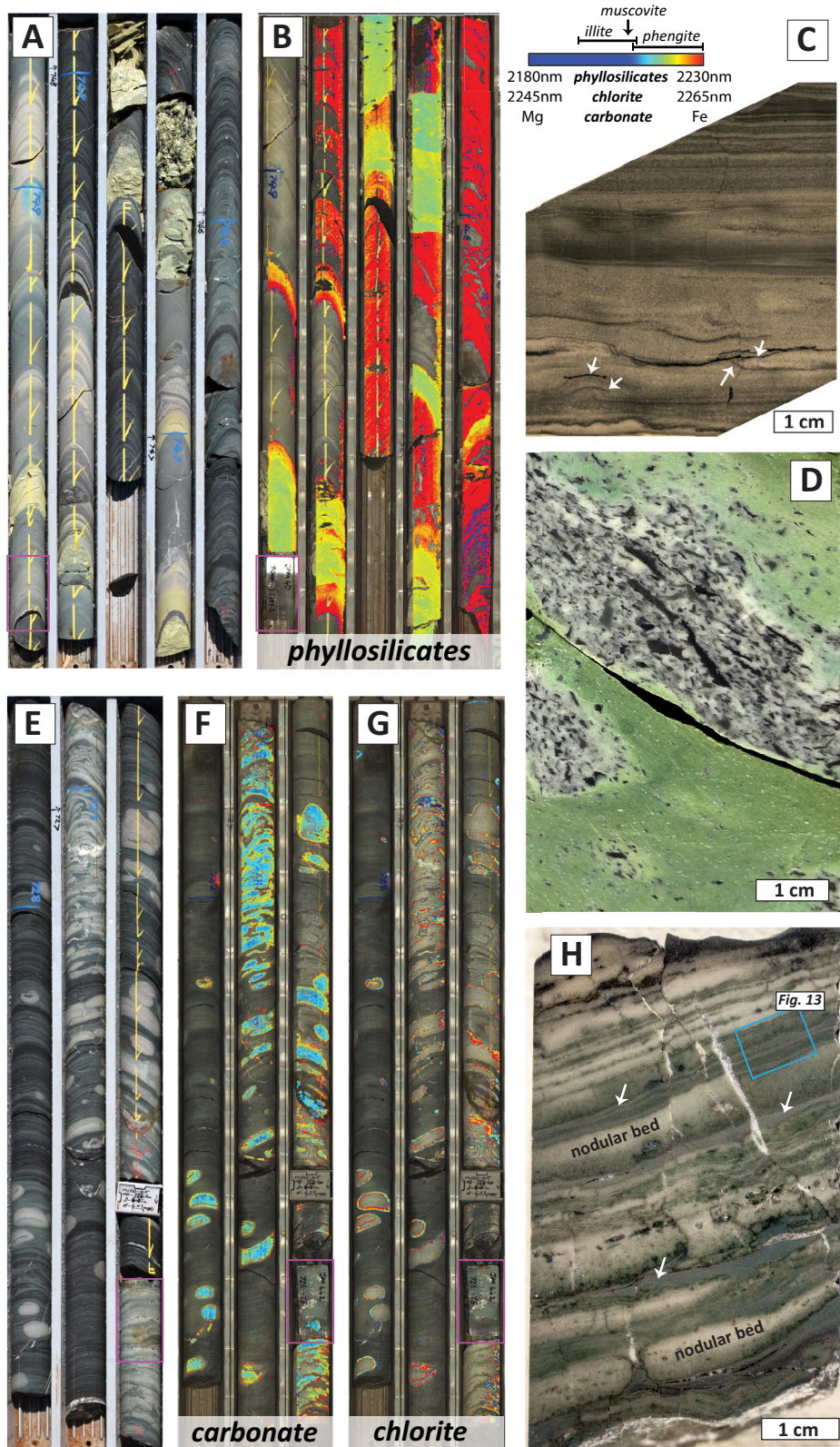| Sample	Drill hole	Meters	S1 (mg/g)	S2 (mg/g)	S3 (mg/g)	Tmax (°C)	HI (mg HC/g TOC)	OI (mg CO2/g TOC)	TOC (%)°	Ro
JM137	TNDD015	551.5	0.24	0.47	1.11	484	11	25	4.4	1.6
JM162	TNDD012	560.0	0.06	0.23	0.31	496	11	15	2.12	1.8
JM173	TNDD019	884.2	0.05	0.09	0.17	472	7	14	1.2	1.3
JM210	TNDD015	251.4	0.69	0.91	0.17	448	44	8	2.09	0.9

TOC = total organic carbon

Fig. 10. Corescan™ hyperspectral imaging of core boxes from TNDD015. (A). Core box photograph: 746 to 753 m. (B). Phyllosilicate mineralogy (spectral wavelength) for same interval as (A). (C). Hand sample photograph of JM40, showing a volcaniclastic sandstone bed with flame structures and mud drapes annotated with white arrows. (D). Pervasive and texturally destructive green illite alteration of a mud-chip, volcaniclastic sandstone bed. (E). Core box photograph: 726 to 729 m. (F). Carbonate and (G) chlorite spectral responses for same interval as (D). (H). Hand sample photograph of JM42, showing chlorite alteration of dolomite nodules and mudstone laminations (white arrows). Blue box highlights area shown in Figure 13.
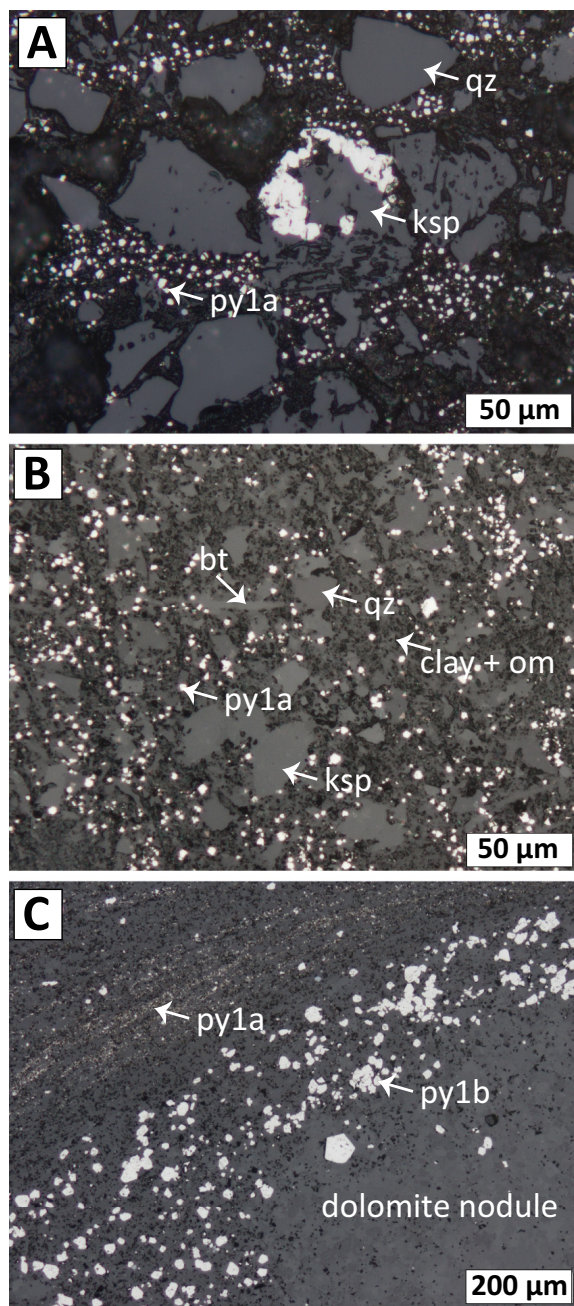
Fig. 11. Reflected light photomicrographs of pyrite textures in the Lower HYC unit. (A). Fine-grained pyrite (py1a) within the carbonaceous matrix of a silty-mudstone sample (JM202). The clasts are a mixture of quartz (qz) and K-feldspar (ksp). The K-feldspar clast in the center of image is partially dissolved and replaced by pyrite. (B). Disseminated pyrite (py1a) within a matrix-supported carbonaceous mudstone (JM132). As in (A), clasts are predominantly quartz (qz) and K-feldspar (ksp) with minor biotite (bt). (C). Dolomite nodule with euhedral pyrite (py1b) concentrated around its margin.

chlorite alteration are distributed independently of zones of sulfide mineralization, which suggests the two assemblages did not form concurrently (e.g., Fig. 16D, E).

In the Main lens of the Lower HYC unit (mode 2), sphalerite and galena form a fine-grained cement that exploited multiple types of porosity, which is predominantly stratiform but locally also crosscuts bedding (e.g., Hayward et al., 2021, fig. 7). In the carbonaceous mudstones that are immediately adjacent to volcaniclastic sandstone beds, sulfides preferentially replaced K-feldspar (Fig. 17). Away from the volcaniclastic sandstone beds, and representative of the bulk of higher grade stratiform Main lens mineralization, sphalerite and galena were precipitated in: (1) interparticle pore space of stratabound aggregates of pyrite and phyllosilicate matrix (e.g., Fig. 15), and (2) intramineral pore space associated with dolomite and K-feldspar dissolution (e.g., Fig. 17).

Discussion

There are clear compositional end members in the lithogeochemical dataset (Fig. 6), which when combined with the petrographic dataset can be used to interpret the siliciclastic, diagenetic, and hydrothermal evolution of the Teena subbasin. The following discussion, therefore, focuses on answering three main questions: (1) What was the primary composition of the Lower HYC unit in the Teena subbasin? (2) What is the relationship between diagenetic phases (e.g., hematite, chlorite, illite, feldspar) and sulfides in the Lower HYC unit? (3) What were the main factors controlling sulfide mineralization in the Lower HYC unit?

Primary host-rock composition

In siliciclastic rocks, the mineralogical composition of detrital input provides a 1st-order control on protolith composition and the mineral assemblages that develop both during diagenesis and also during hydrothermal alteration. Dolomite also forms massive dolostone beds in the Teena subbasin, although how much of this dolomite is primary is difficult to establish following the widespread diagenetic recrystallization (Hayward et al., 2021). This is encapsulated by the W-Fold Shale Member, which is a transitional unit between the Teena Dolostone and the Lower HYC unit (diagenetic dolomite, e.g., Fig. 16B). The W-Fold Shale Member contains a mixture of dolostone interbeds, diagenetic nodules, and interbedded siltstones, which are represented by contrasting PC2 values (Fig. 6C). Some samples from the overlying Lower HYC unit do contain thin dolostone interbeds that are comparable to the W-Fold Shale Member (Fig. 6C), but the general trend is toward more siliciclastic compositions.

Immobile elements (K, Ti) provide a good proxy for lithologic variability in the siliciclastic end member (e.g., Fig. 6E). For example, the primary detrital trend is represented by co-variation between K and Ti that is broadly consistent in all the major lithologic units in the Teena subbasin. The XRD data show that potassium feldspar is a major component of the samples in this primary detrital trend, which is consistent with other studies on the Barney Creek Formation (e.g., Baruch et al., 2015). Importantly, however, there is a subgroup of high K outliers, primarily from the W-Fold Shale Member and Lower HYC unit, which plot away from this primary detrital trend and represent samples from volcaniclastic sandstone

abound aggregates, whereas the sphalerite and galena form 2 primary modes. In the Lower lens of the Lower HYC unit (mode 1), the sphalerite and galena are primarily associated with the replacement of nodular dolomite (e.g., Figs. 4B, 16). There is weak chlorite alteration of dolomite nodules in some of the mineralized samples in the Lower HYC unit. Zones of
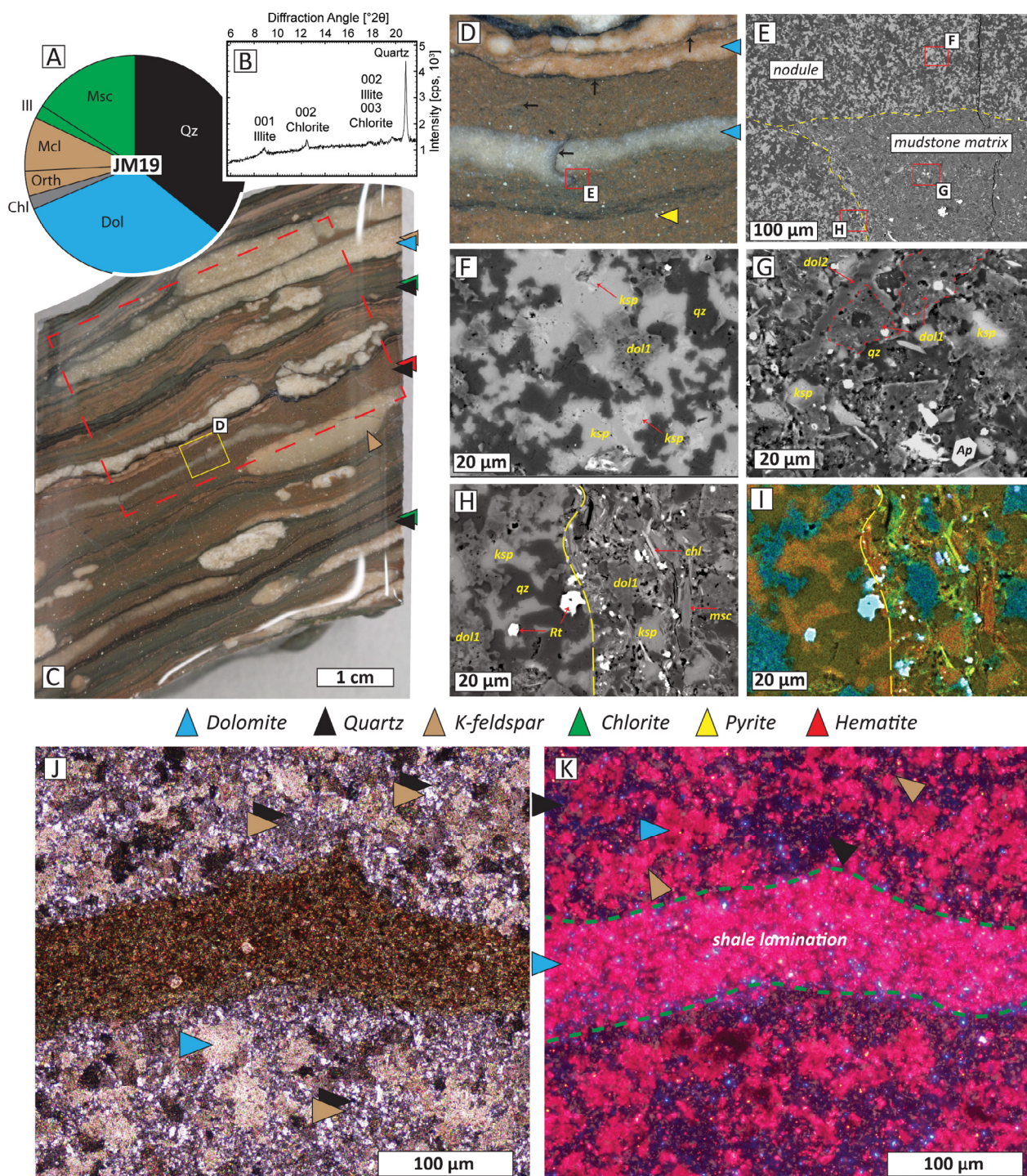
Fig. 12. (A). Bulk mineralogy of hand sample (C). (B). Clay fraction analysis of sample shown in (C). (C). Hand sample photograph from the W-Fold Shale Member (JM19 @ 850 m; TNDD015). (D). Binocular photomicrograph of the area highlighted in (C), showing hematite alteration within both nodular dolomite and the adjoining mudstone laminations (stylolitic horizons are denoted by black arrows). (E). Backscatter electron (BSE) image of inset from (D), showing the interface between mudstone lamination and nodule. Higher resolution images follow for the annotated insets (red boxes). (F). Dolomite nodule alteration assemblage of K-feldspar (ksp) and quartz (qz). (G). BSE image of the fine-grained mineralogy of the mudstone lamination, in which dolomite cement (outlined in red) contains hematite microinclusions that show up as white spots of high BSE reflectance and result in the characteristic red coloration in hand sample. (H). BSE image of the interface (yellow line) between the altered dolomite nodule and mudstone lamination. (I). False color electron dispersive X-ray (EDX) map for the area shown in (H). Notice the distribution of dolomite (turquoise) within both the nodule and as cement in the mudstone lamination. (J) and (K) show cross polar and cathodoluminescence images of mudstone lamination and adjacent nodular dolomite with K-feldspar alteration. Ap = apatite, Chl = chlorite, Dol = dolomite, Ill = illite, ksp = K-feldspar, Mcr = microcline, Msc = muscovite, Orth = orthoclase, Qz = quartz.
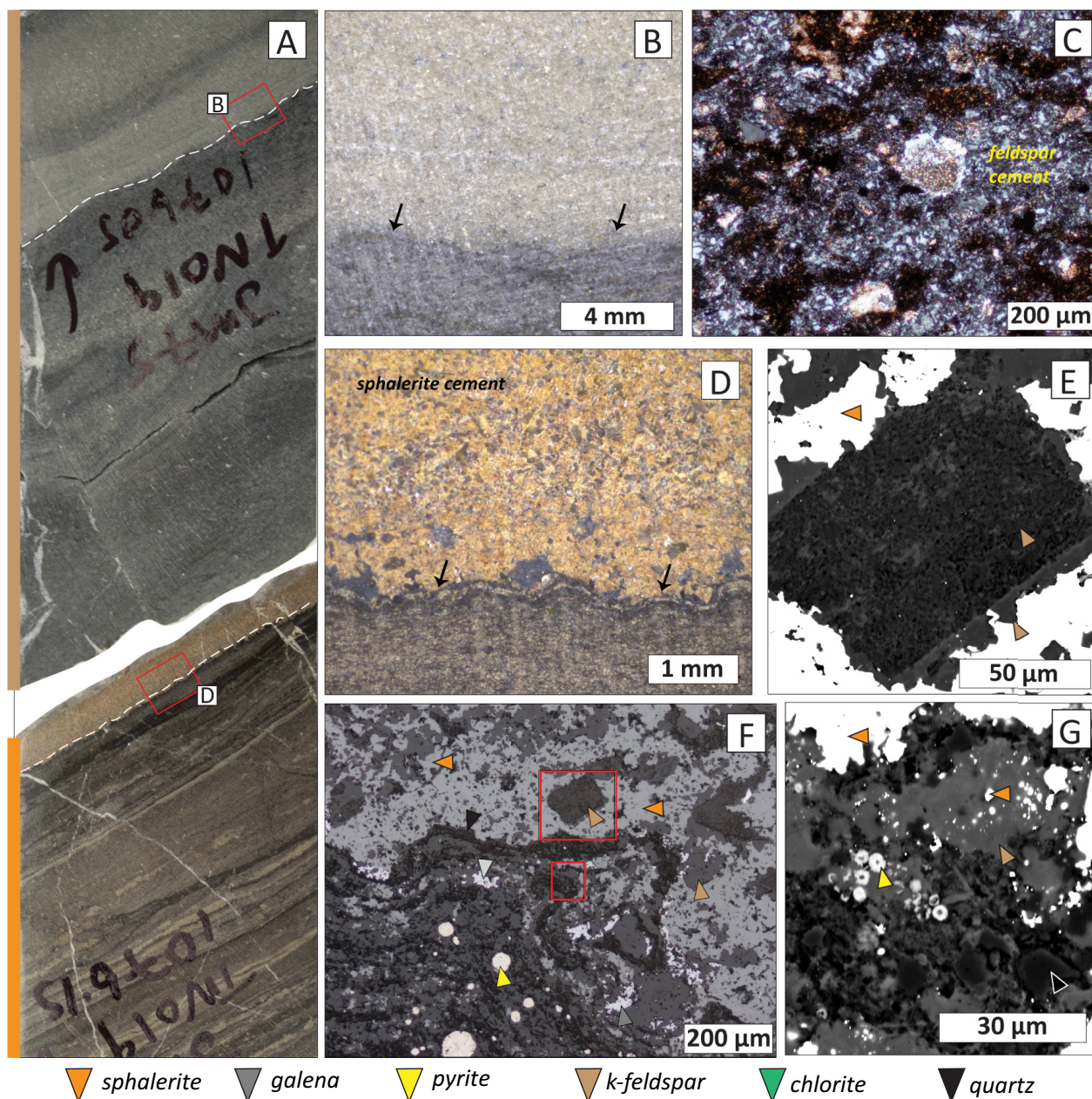
Fig. 13. (A). Hand sample photograph of mineralized carbonaceous mudstone and overlying volcaniclastic sandstone bed (Lower HYC unit 1076.0-1076.2 m in TNDD019; JM75). (B). Binocular photomicrograph of red box in (A). (C). Transmitted light photomicrograph (crossed polar), showing the fine-grained groundmass of anhedral K-feldspar + quartz grains, with patchy phyllosilicates, dolomite, and coarser grained clast (e.g., center) comprising remaining field of view. (D). Binocular photomicrograph of area highlighted by red box in (A), in which sphalerite mineralization forms the main matrix phase in the base of a volcaniclastic sandstone bed. (E). A euhedral clast of K-feldspar with a trachytic texture characteristic of a volcanic origin. The clast is overgrown by authigenic K-feldspar, which has undergone partial replacement by sphalerite (sp) as preserved by the irregular (saw tooth) caries texture. (F). A reflected light image of the erosive contact between the carbonaceous mudstone and volcaniclastic sandstone bed. (G). The partial replacement of authigenic K-feldspar by sphalerite in the mineralized carbonaceous mudstone.

beds (e.g., Fig. 6E). Some of the clasts from the volcaniclastic sandstone beds preserve trachytic textures that are consistent with a volcanic origin (e.g., Fig. 13E). Previous studies in the Glyde subbasin, ~110 km south of Teena, interpreted volcaniclastic sandstone and shale beds in that subbasin to be subaqueous pyroclastic flow deposits and ashfall tuff deposits, with volcanic input linked to distal felsic igneous activity dur-

ing deposition of the Barney Creek Formation (Jackson et al., 1987; Davidson and Dashlooty, 1993). In the Teena subbasin, the sedimentological features of the volcaniclastic sandstone beds are consistent with deposition via submarine turbidity currents (mass flow) and slump processes (see rip-up clasts, erosive contacts, mud chip fragments, flame structures, normal-graded successions; e.g., Fig. 10C).
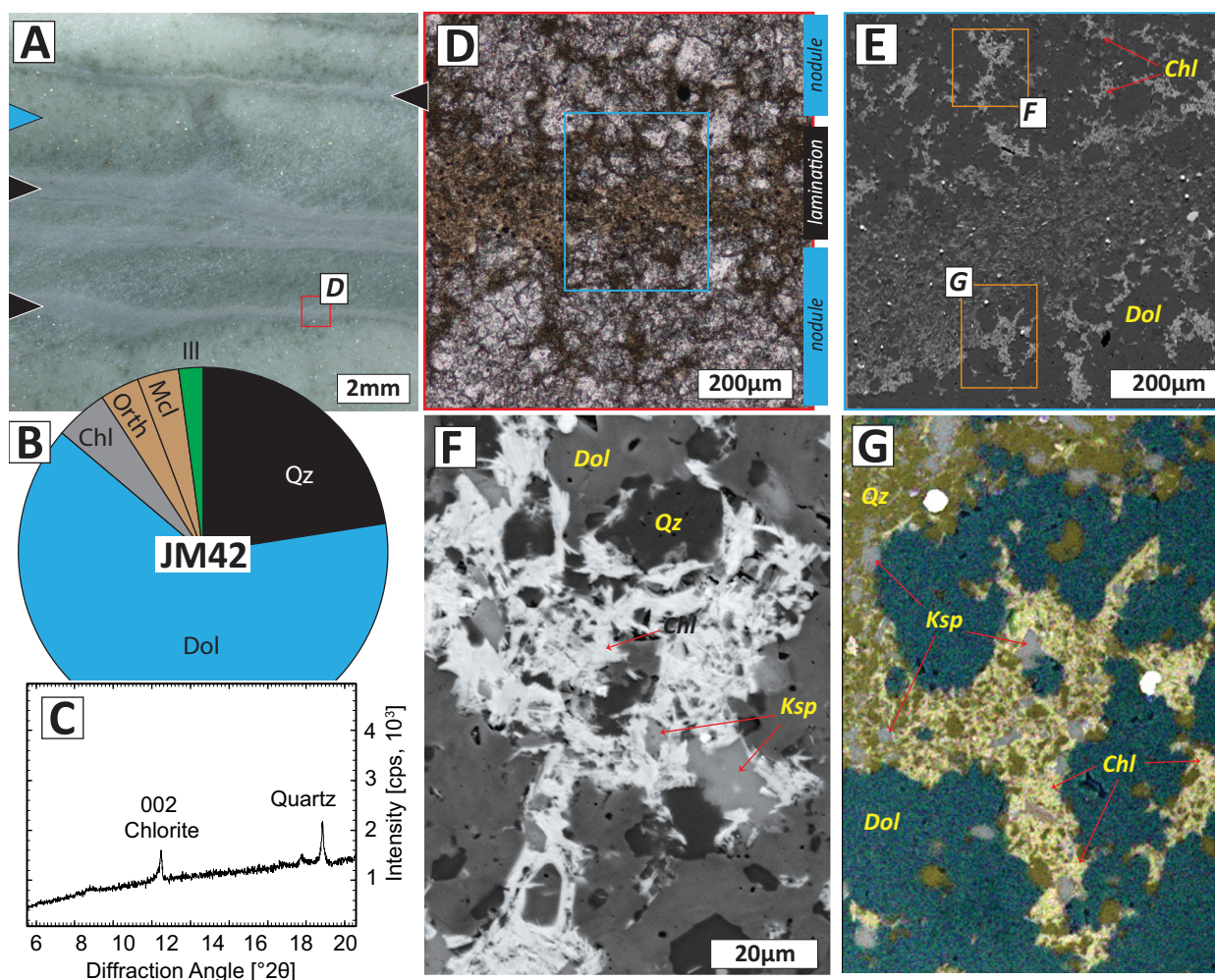
Fig. 14. (A). Binocular photomicrograph of the area highlighted in Figure 10H. (B). Bulk mineralogy of hand sample shown in (A). This image shows the chlorite (green) alteration of nodular dolomite forms sharp contacts with interlaminated mudstone. (C). Clay fraction analysis of sample shown in (B). (D). Transmitted light photomicrograph of area highlighted in (A), showing chlorite formation interstitial to nodular dolomite either side of the mudstone lamination. Blue box represents area shown in (A), which shows a BSE image of the interface between the mudstone lamination and nodular dolomite. (F). BSE image of assemblage associated with nodule dissolution and chlorite formation. Fibrous chlorite is the dominant phase with minor K-feldspar and quartz. (G). False color electron dispersive X-ray (EDX) map of another example of the interface between nodular dolomite and mudstone lamination, showing the distribution of chlorite + quartz + K-feldspar (the high response phase is pyrite). See Figure 12 for abbreviations.

Overall, the broad similarity in the immobile element composition of the W-Fold Shale Member, Lower, Middle, and Upper HYC units indicates that a large proportion of the Barney Creek Formation can be described by a primary detrital trend of immature arkosic siltstones and mudstones that have been variably affected by dolomitization. The volcaniclastic sandstone beds are a minor but important component of the W-Fold Shale Member and Lower HYC unit and can be identified as outliers from the primary detrital trend (Fig. 6E), interpreted to be less mature mass-flow units of similar provenance.

Diagenesis in the W-Fold Shale Member

One of the most distinctive features of the W-Fold Shale Member is the red and green layering (e.g., Fig. 12), which has also been described in a number of subbasins in the McArthur Basin (McGoldrick et al., 2010). The red and green coloration has previously been linked to changes in the valency of Fe that was controlled by redox stratification of the water column (Large et al., 1998). The stratified water column model implies that the distribution of the Fe-bearing phases was controlled by depositional redox conditions.

In the Teena subbasin, the red coloration in the W-Fold Shale Member is most likely associated with hematite inclusions in the dolomite cement (e.g., hematite is enclosed within the red outline highlighting dolomite cement; Fig. 12G). Dolomite cement with hematite inclusions has an irregular and patchy distribution in the W-Fold Shale Member and locally penetrates down to at least 50 m deep in the underlying Teena Dolostone. Considering the discordant stratigraphic distribution and the spatial association with dolomite cement, hematite precipitation is considered to have postdated sedimenta-
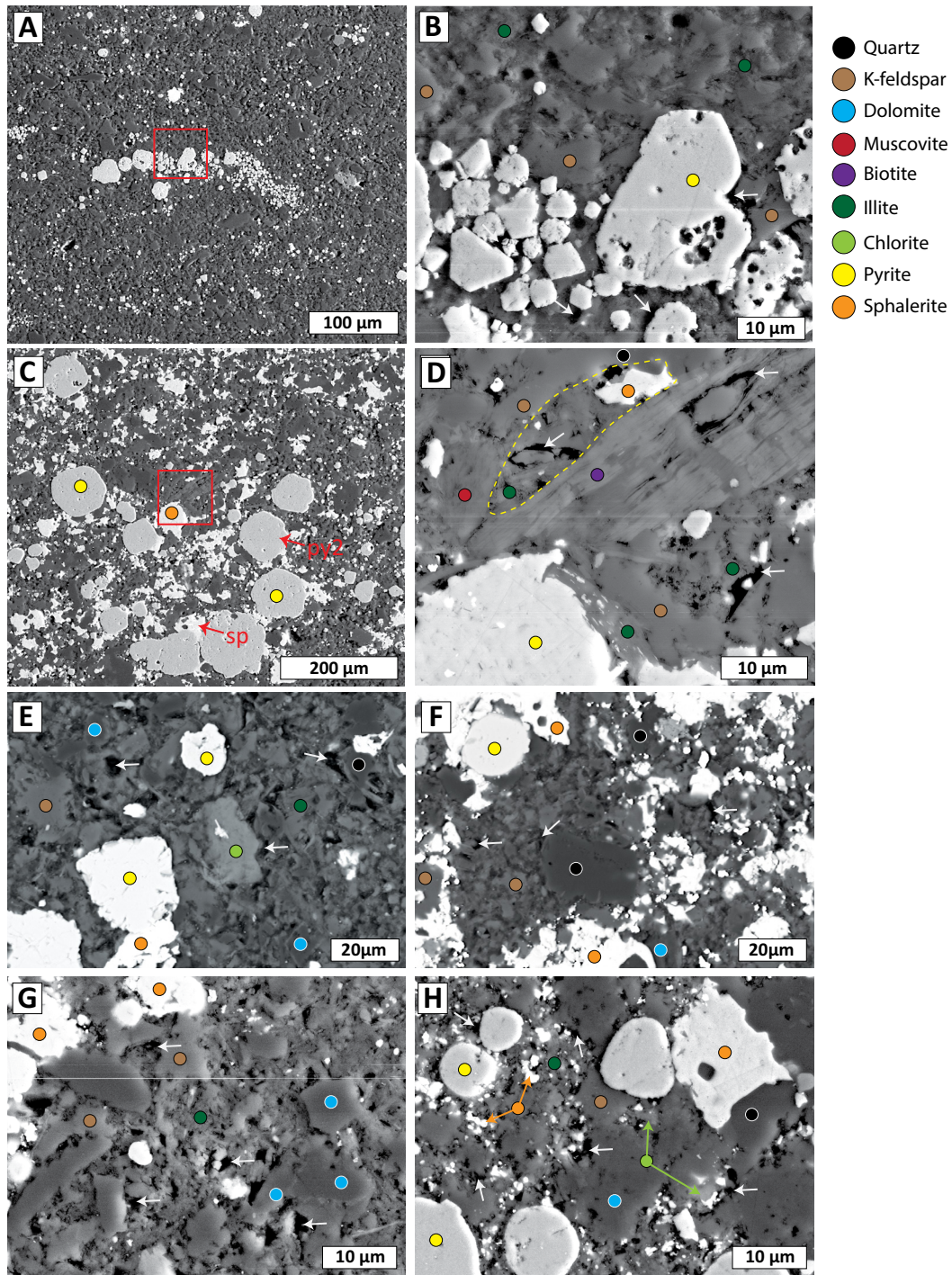
Fig. 15. Back-scatter electron (BSE) photomicrographs of the siliciclastic matrix of samples from the Lower HYC unit in TNDD019 (A, B, C, D = JM79B @ 1,064 m; E, F = JM72 @ 1,083 m; G, H = JM73 @ 1,080 m). Colored circles represent spots selected from compositional analyses (EDS). (A). An aggregate of py1a overgrown by larger crystals of hydrothermal pyrite (py2). The remainder of the sample mostly comprises matrix-supported detrital clasts of quartz and K-feldspar. The red box highlights the area shown in (B). (B). Close-up detail of the area outlined in (A) where the fine-grained amorphous phase that forms the cement to the clasts is illite. White arrows indicate secondary pore spaces developed within mineral aggregates (illite) or at crystal boundaries (pyrite). (C). Sphalerite mineralization (palest gray) within the fine-grained matrix. (D). Image shows the area outlined in (C) with sphalerite mineralization associated with pore space in which illite has formed (yellow dashed line). (E). Image shows large sphalerite and pyrite crystals set within a matrix of illite and chlorite (with minor quartz and dolomite) that preserves interparticle pore space (white arrows; JM72). (F). Image shows more pervasive fine-grained sphalerite mineralization that appears to have exploited the interparticle pore space preserved within the mudstone matrix. (G). Image shows interparticle pore space (white arrows) within the siliciclastic matrix. The sample contains irregular clasts of K-feldspar and dolomite that are set within a matrix of illite-smectite. (H). Image shows large crystals of pyrite and sphalerite together with fine-grained sphalerite cement within pore space preserved within the phyllosilicate assemblage.
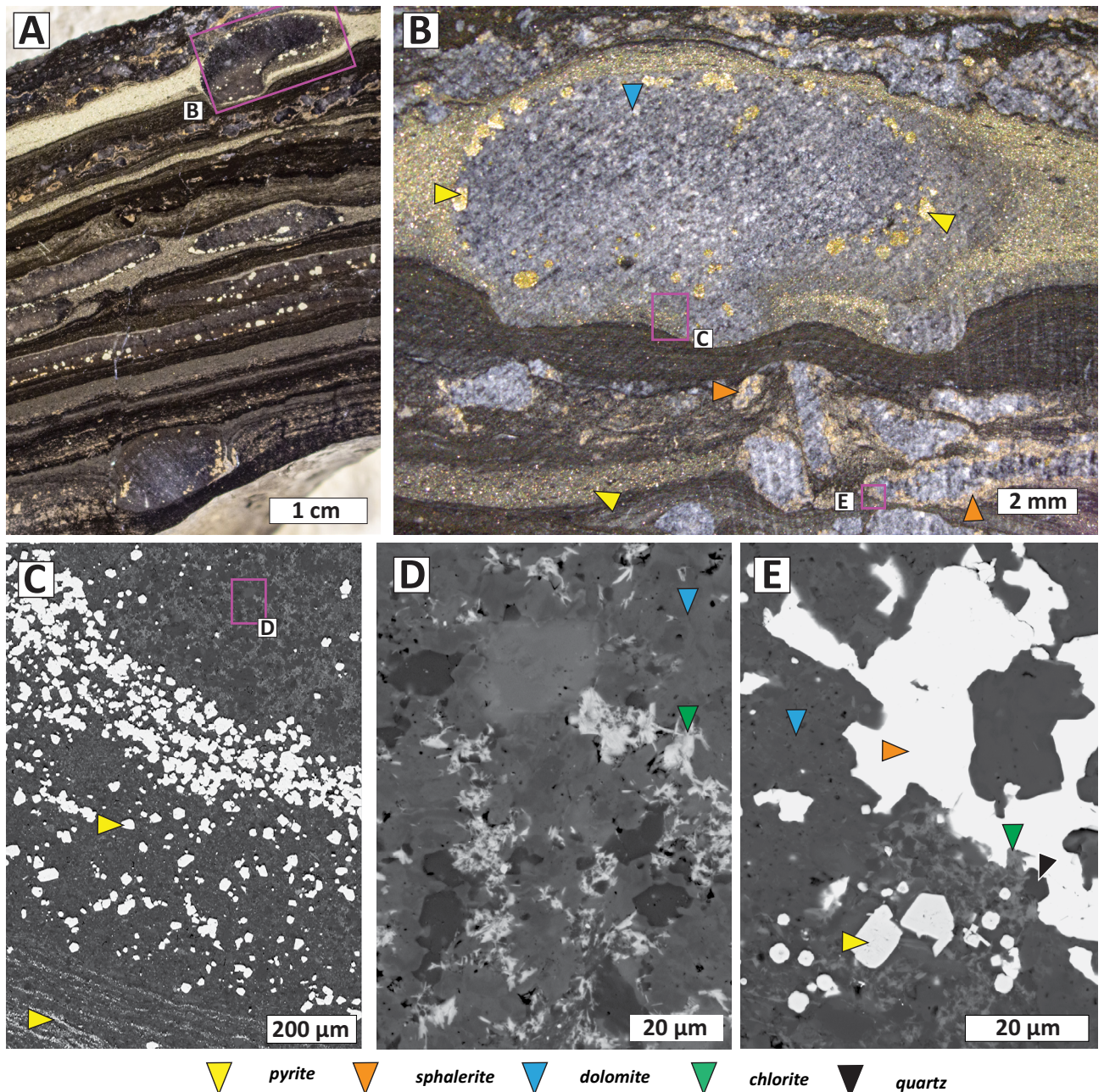
Fig 16. (A). Hand sample from the bottom of the Lower HYC unit (JM63 @ 1,182 m TNDD019), showing weak mineralization and dolomite nodule growth and to have formed as an alteration phase during eogenesis. Either this means that the in a sample containing nodular dolomite and fine-grained pyrite (py1). (B). Large dolomite nodule with idiomorphic py1b concentrated around margin. The smaller irregular nodules in lower half of the image have been partially replaced by sphalerite. (C). A BSE image of a section of the dolomite nodule highlighted in (B), showing the py1b crystals concentrated around the margin. (D). Chlorite neoformation within the dolomite nodule. (E). Sphalerite replacement of the small dolomite nodules. There is also weak chlorite alteration in this image, but it appears to form independently of sphalerite (see D).

tion and dolomite nodule growth and to have formed as an alteration phase during eogenesis. Either this means that the in situ eogenetic fluids (i.e., modified seawater) were oxidizing, or that there was an influx of oxidizing fluids from elsewhere (e.g., Morad et al., 2000). The two options are not mutually exclusive, considering that in situ oxidized fluids would still flow down hydraulic gradients associated with basin subsidence.

The characteristic green color in the W-Fold Shale Member is associated with chlorite (e.g., Fig. 14). Chlorite can form at relatively low temperatures during mesogenesis (e.g., 40°–120°C for Fe chlorite, >100 °C for Mg chlorite; Beaufort et al., 2015), as well as at higher temperatures during late-stage diagenesis and metamorphism. The bladed, pore-filling morphology of the chlorite that is interstitial to dolomite nodules (e.g., Fig. 14F) is typical of the Fe-rich end member (cf. Beaufort et al., 2015), whereas the hyperspectral imaging records both Mg- and Fe-rich end members (Fig. 10G). Altogether, it is likely that chlorite formed over a range of diage-
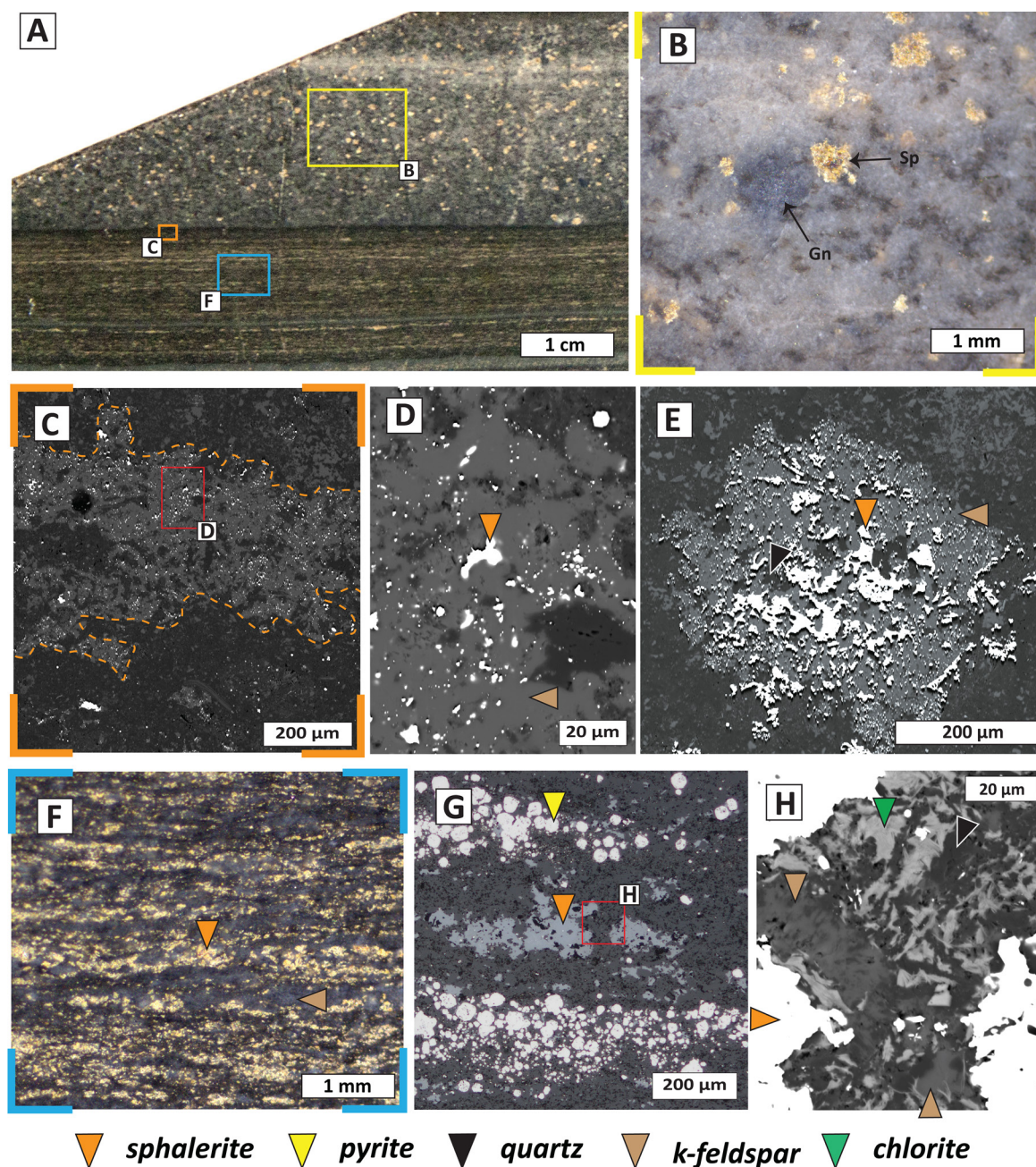
Fig. 17. (A). Hand sample from a mineralized volcaniclastic sandstone bed in TNDD019 (1,124 m) in which patchy mineralization within the sandstone bed can be compared with the fine-grained stratiform mineralization in the underlying mudstone. (B). Disseminated sphalerite and galena within a quartz and K-feldspar groundmass. (C). BSE image of an area close to the base of the volcaniclastic sandstone bed in (A). As with (B), sphalerite mineralization is associated with partial replacement of K-feldspar (as highlighted by the orange dashed line). There is no sphalerite associated with the quartz groundmass. (D). High resolution BSE image of area in (C), showing the partial replacement of K-feldspar. (E). An image (BSE) of the disseminated sphalerite within the volcaniclastic sandstone bed, showing replacement of a K-feldspar clast. (F). Binocular photomicrograph of the stratiform sphalerite mineralization in the mudstone beneath the volcaniclastic sandstone bed. (G). Stratiform aggregates of py2 together with disseminated sphalerite. (H). High-resolution BSE image of the area shown in (G), where chlorite is associated with the sphalerite + K-feldspar assemblage.

netic stages (i.e., ~40°–200°C, ~2- to 6-km depth) rather than as a distinct paragenetic stage.

Berthierine is an important precursor to diagenetic chlorite formation (Hornibrook and Longstaffe, 1996) and may have been a common phase in the anoxic nonsulfidic (fer-ruginous) conditions that were characteristic of Proterozoic marine environments (Tang et al., 2017; Johnson et al., 2020). In particular, low sulfate availability and variable TOC burial would have limited BSR, meaning that Fe would have been retained within berthierine rather than being transferred to

pyrite. Transformation of berthierine to chlorite would then have occurred via a solid-state transformation during burial diagenesis (Beaufort et al., 2015):

$$2(Fe^{II},Mg,Al)_3(Si,Al)_2O_5(OH)_4 =$$
$$(Fe^{II},Mg,Al,Fe^{III})_6SiAl_4O_{10}(OH)_8. \quad (7)$$
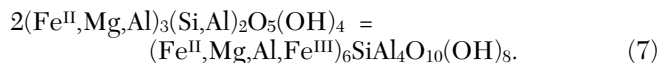
In the lowermost interval of the Lower HYC unit there is petrographic evidence that weak chlorite alteration predated sphalerite mineralization (see Fig. 16D, E that show chlorite alteration distributed independent of sphalerite mineralization vs. sphalerite after chlorite). Higher up in the Lower HYC unit there is no evidence from the hyperspectral imaging of any major chlorite formation associated with sulfide mineralization in the sulfide lenses. Furthermore, lithogeochemical data show that there is no evidence of a difference in the phyllosilicate assemblage when comparing samples from TNDD015 and TNDD019.

In summary, therefore, the red and green alteration that is characteristic of the footwall succession in the W-Fold Shale Member appears to have been the result of contrasting Fe redox chemistry in sulfur deficient fluids that interacted with the sediments during diagenesis. The eogenetic hematite alteration formed under relatively oxidizing open-system conditions and was followed by the mesogenetic transformation of berthierine to chlorite under more closed system conditions.

Potassium metasomatism (eogenesis)

The combination of high K/Al ratios (Fig. 6F) and widespread K-feldspar cement (Fig. 13) in the volcaniclastic sandstone units provides evidence of both higher detrital K-feldspar content and K metasomatism in the Lower HYC unit of TNDD019. A similar assemblage is found in the W-Fold Shale Member, where weaker K metasomatism resulted in partial replacement of dolomite nodules by K-feldspar and quartz (Fig. 12F). There is also evidence of K metasomatism in similar lithotypes from the Barney Creek Formation at the McArthur River deposit and along the Emu fault zone (Davidson, 1999). It is necessary, therefore, to consider the role of K metasomatism in controlling subsurface fluid flow in the Teena subbasin.

The timing of K metasomatism would have determined whether the thickest volcaniclastic sandstone unit between the Main and Lower mineralization lenses formed an aquifer or an aquitard to hydrothermal fluid flow. The Zn + Pb grades decrease with vertical distance from the upper and lower margins of the coarse-grained volcaniclastic sandstone beds that separate the main sulfide lenses in the Lower HYC unit. The sandstones beds are not mineralized, except in thin intervals adjacent to contacts with carbonaceous interbeds. There is good petrographic evidence that sulfide mineralization locally replaced both detrital and authigenic feldspar (e.g., Fig. 13), although this process did not occur throughout the feldspar-rich volcaniclastic sandstone beds. If feldspar cementation predated sulfide mineralization in the volcaniclastic unit, it could have formed an aquitard to the hydrothermal mineralizing fluids, such that mineralizing fluids were preferentially channeled along the aquitard contacts. The selective replacement of K-feldspar by sulfides occurred only in some thin volcaniclastic sandstone interbeds and was probably controlled by a combination of reduced sulfur availability and the local-

ized generation of acid, both of which could have been linked to the hydrothermal degradation of organic matter within the host rock.

The petrographic evidence that shows feldspar authigenesis predated sulfide mineralization in the Teena subbasin is consistent with the model of Davidson (1999) for the McArthur River district. Using a combination of modal mineralogy and bulk-rock $\delta^{18}O$ values, Davidson (1999) showed that feldspar authigenesis was derived from low-temperature ($32° \pm 27°C$) saline fluids mobilized during tectonic activity. A similar model is favored in the Teena subbasin as the highest K/Al ratios are preserved in TNDD019 (Fig. 6F), which is consistent with fault bound rather than basin margin input.

Illite and phengite

The main phyllosilicate phases in the samples from the Lower HYC unit are illite and phengite (Fig. 8). In most sedimentary basins illite typically forms as a prograde reaction product through the gradual transformation of dioctahedral smectite (Lynch, 1997):

$$Smectite + K^+ = illite + SiO_2 + H_2O. \quad (8)$$

Provided there is a source and sink for K and Si, illitization of smectite is complete by ~120°C and will then gradually evolve to phengite and eventually muscovite (Hower et al., 1976; Merriman and Peacor, 1998). The abundance of detrital clay minerals is thought to have been much lower during the Proterozoic due to lower levels of chemical weathering (Rafiei and Kennedy, 2019). Nevertheless, the immature volcaniclastic composition of siliciclastic input into the Teena subbasin means that smectite would either have been a major detrital phase or present as an alteration product of volcanic glass. Many of the volcaniclastic sandstone beds fine upward and contain a high proportion of immature, smectite-rich material, which is now present as illite-rich volcaniclastic siltstone and claystone beds.

With increasing temperature and pressure, changes in the crystallite thickness and lattice strain of illite result in a narrowing of the 10 Å peak (Weaver, 1960). Measurements of illite crystallinity across a range of diagenetic conditions are classified by the Kübler index for subgreenschist facies rocks (e.g., Abad, 2007; Warr and Cox, 2016). The more carbonaceous and K-feldspar rich samples (e.g., Middle HYC unit and volcaniclastic sandstone beds) contain illite with lower degrees of crystallinity, whereas the more carbonate rich lithologies (e.g., W-Fold Shale Member) preserve higher crystallinity (Fig. 9). This observation implies that the relative availability of K influenced the timing and therefore crystallinity of illite growth. Overall, the illite crystallinity indicates that illite formed throughout diagenesis, initially at relatively low temperature (100°C) in K-rich siliciclastic rocks. Illite formation was later in more carbonate rich rocks, at higher anchizone and epizone temperatures (<300°C; Fig. 9), which highlights differences in how carbonate and siliciclastic rocks behaved during diagenesis. In this case, illite formation in the samples containing a greater proportion of carbonate would likely have been retarded due to the diminished availability of K and Al during early diagenesis (e.g., Alonso-Azcarate et al., 1995).

Despite the formation of illite over a wide range of temperatures, there is no evidence of major paragenetic overlap with

sulfide mineralization in the Lower HYC unit. Furthermore, in a comparison of samples from the Lower HYC unit, which hosts the main mineralization lenses, there is no zonation in either illite abundance or crystallinity between TNDD015 and TNDD019 (Fig. 9). In contrast, smectite is preserved in samples from the mineralized drill holes (TNDD012 and TNDD019), which is typical of retrogressive alteration of preexisting illite (Nieto et al., 1994). Retrogressive alteration could develop during postorogenic exhumation (i.e., telogenesis); however, considering the restriction to samples collected several hundred meters below surface from TNDD019, it seems more likely that a small amount of retrogressive smectite was formed as an alteration product as the hydrothermal system waned.

The chemical mass balance of dolomite replacement sulfide mineralization in the Lower HYC unit

There is strong petrographic evidence that sulfides replaced dolomite in the Teena subbasin (e.g., Fig. 4B). There is a notable difference in dolomite abundance between the Lower HYC unit in TNDD015 and TNDD019 (Figs. 6, 7), which either (1) indicates a lower abundance of dolomite in TNDD019, or (2) provides further evidence of dolomite replacement during sulfide mineralization. An original decreased abundance of carbonate is suggested by the lower abundance of dolomite nodule textures in the higher grade Main lens mineralization in TNDD019, perhaps as the result of decreased carbonate deposition in the deeper water facies of the subbasin depocenter (Hayward et al., 2021). However, this does not preclude that sulfide replacement of the dolomite cement occurred as well, which could explain the characteristic fine-grained sphalerite cement (Fig. 4; also cf. Spinks et al., 2021).

Attempts to overcome such ambiguous petrographic observations often involve an evaluation of chemical mass balance in bulk-rock lithogeochemical data (Wilkinson et al., 2011; Rieger et al., 2021). Most geochemical techniques used for evaluating protolith alteration require accurate reference values and the careful selection of appropriate immobile elements (Grant, 1986; Humphris et al., 1998). At the McArthur River (HYC) deposit, previous attempts to evaluate the mass balance of carbonate replacement have produced conflicting results (Hinman, 2001; Ireland et al., 2004). For example, Hinman (2001) conducted a Gresens' analysis that showed <45% loss of carbonate in samples from the McArthur River (HYC) ore zone. The reference value used in this analysis, however, was a dolomitic siltstone sample located more than 20 km from the McArthur River (HYC) deposit, and so may not accurately represent the protolith at McArthur River (HYC) deposit (Ireland et al., 2004). Instead, Ireland et al., (2004) applied a similar method using a reference value containing less dolomite, which was derived from the average composition of a suite of unmineralized centimeter-scale siltstone beds that are interbedded with sulfide-bearing beds at the McArthur River (HYC) deposit. Using this reference value there is no evidence of carbonate loss, yet it does not preclude the possibility that the interbedded siltstones are unmineralized precisely because of a lack of preexisting nodular carbonate. Indeed, recent work on the ore zone at the McArthur River (HYC) deposit has now provided more convincing

petrographic evidence of widespread sulfide replacement of carbonate (Spinks et al., 2021).

In the Teena subbasin, the samples used for calculating reference values were screened for outliers that are associated with variable protolith compositions (i.e. volcaniclastic sandstone beds; Fig. 6E). The similarity of the immobile elements in the remaining samples provides the best evidence of similar protolith composition in the unaltered and altered reference values. Importantly, the Gresens' analysis provided no evidence of major mass gain in the mineralized samples, which rules out the possibility that Zn has simply diluted all other components of the protolith (i.e., represents a closure effect). This means that the correlation between Ca_{loss} and Zn concentration in the Main lens of TNDD019 could be considered in terms of the molar volume ratio of dolomite replacement by sphalerite (1:2.7; Fig 8F). The high Ca_{loss} and low Zn samples (Fig. 8F) represent those samples that are outliers to the primary detrital trend (Fig. 6E). The overestimation of Ca_{loss}, therefore, is the result of lower Ti concentrations in the volcaniclastic sandstone beds that are interspersed through the Lower HYC unit.

The overall importance of dolomite replacement should be considered in terms of the scale of the lithogeochemical sampling, which was continuous at 30-cm intervals through the mineralized lenses in the Lower HYC unit. This means that the samples falling along the dolomite replacement trend provide robust evidence of dolomite replacement at a large scale (decimeter to meter scale). Importantly, however, the non-zero intercept of the regression between Ca_{loss} and Zn concentration for samples from the Main lens does indicate that a substantial fraction of the Zn (~1 mol/kg) could have formed via other modes of host-rock replacement. For example, there is good petrographic evidence of feldspar replacement within thin sandstone beds among dolomitic siltstone in the Lower HYC unit (e.g., Fig. 13). The volcaniclastic sandstone beds are thickest in TNDD019, which intersects the depocenter of the Teena subbasin (Hayward et al., 2021). These samples are mostly unmineralized, and due to being low Ti outliers of the primary detrital trend (Fig. 6E), there is also an overestimation of Ca_{loss} (Fig. 8F). In other drill holes away from the subbasin depocenter the sandstone beds are more thinly interbedded with the beds containing sulfides (Hayward et al., 2021). This means that at the scale of the sampling (i.e., 30-cm intervals), the chemical mass balance model is more complicated where samples are not so well represented by the Main lens and volcaniclastic sandstone beds from TNDD019 (e.g., TNDD012; Fig. 8F). In these drill holes, therefore, the extent to which mineralization resulted in replacement of both dolomite and K-feldspar is less clear.

Altogether, the mixture of dolomite, K-feldspar and organic carbon in the Lower HYC unit would have served as an effective batch reactor during burial diagenesis and the onset of hydrothermal activity. Considering the immature nature of the siliciclastic input to the Teena subbasin, some interclast primary porosity was likely to have been retained during sediment burial. If mineralization was emplaced <1-km depth, as proposed by Hayward et al (2021), the organic matter in the host rock would be evolving toward the kerogen + CH_4 window (i.e., 80°–180°C; Bernard and Horsfield, 2014). During these early stages of burial diagenesis, primary crack-

ing of kerogen might have generated sour gas ($H_2S \pm CH_4$-CO_2) that could have resided within primary pore spaces. In some of the finer grained carbonaceous beds the formation of fine-grained sphalerite cement has exploited micrometer-scale matrix-related pore space (Fig. 15). This pore space could have been occupied by a fine-grained dolomite cement that was subsequently replaced or leached out, but it could also have contained organic components. At higher temperatures (>180°C) organic matter maturation could have been hydrothermally forced, thereby resulting in local oil generation (e.g., Broadbent et al., 1998). This is consistent with the higher organic maturities that are preserved within the mineralized subbasins in the Batten fault zone (Fig. 9B; Crick et al., 1988; Baruch et al., 2015). In any case, the Lower HYC unit would have contained an effective in situ reductant and a reactive host rock, which during interaction with a metal bearing fluid had the capacity to produce sulfide mineralization via host-rock replacement.

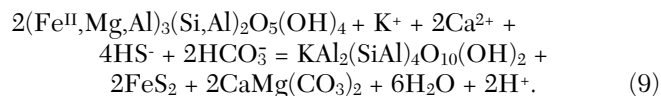### Alteration models for the Teena dolomite replacement system

The lithologic and compositional variability in the Teena subbasin has resulted in a variety of diagenetic and hydrothermal assemblages that have very different characteristics across the footwall and hanging-wall stratigraphy (Figs. 4D, 18).

Footwall alteration: The most distinctive features in the footwall stratigraphy are the hydrothermal dolostone lenses and associated wall-rock recrystallization of carbonate nodules to silica-dolomite aggregates (Fig. 18D), although this may be atypical of CD-type deposits (Hayward et al., 2021). Most of the remaining oxide and silicate assemblages in the footwall stratigraphy (e.g., hematite, K-feldspar, chlorite, illite) record relatively low temperature fluid-rock interactions (Fig. 18A, B) that predated both Zn mineralization and HTD alteration.

In the W-Fold Shale Member the distribution of the different phyllosilicate phases (chlorite, illite) was controlled primarily by closed-system mass transfer due to small-scale compositional heterogeneities in the protolith. For example, there is evidence that chlorite formation is linked with carbonate dissolution in the W-Fold Shale Member, which seems to be associated with dehydration in adjacent siltstone laminations (e.g., Fig. 14). This provides a good example of how secondary porosity might develop in lithologies of mixed siliciclastic and dolomitic compositions undergoing burial diagenesis. In the Lower HYC unit, carbonate nodules are similarly widely recrystallized with some quartz replacement; however, considering the evidence of carbonate replacement by sulfide mineralization it is interesting that there is no discernible phyllosilicate alteration halo.

The absence of chlorite alteration in the Lower HYC unit of the Teena subbasin is consistent with other Carpentaria Zn deposits (e.g., Century, Whitbread, 2004; George Fisher, Rieger et al., 2021). In the Lower HYC unit, which is more carbonaceous than the underlying W-Fold Shale Member, the increased availability of reduced sulfur would have favored the formation of pyrite over berthierine, which is a precursor to diagenetic chlorite formation (e.g., Rieger et al., 2021). Reduced sulfur in CD-type systems either (1) derives from more reduced depositional facies, or (2) is generated during hydrothermal activity. If hydrothermal activity predated diagenetic

chlorite formation in the Teena subbasin, any reactive Fe in berthierine would instead be incorporated into pyrite rather than chlorite. The absence of chlorite in CD-type deposits judged to have formed via subseafloor carbonate replacement, therefore, might be considered in terms of berthierine alteration:

$$2(Fe^{II},Mg,Al)_3(Si,Al)_2O_5(OH)_4 + K^+ + 2Ca^{2+} + $$
$$4HS^- + 2HCO_3^- = KAl_2(SiAl)_4O_{10}(OH)_2 + $$
$$2FeS_2 + 2CaMg(CO_3)_2 + 6H_2O + 2H^+. \qquad (9)$$

As written, this reaction does result in some illite formation (+ pyrite and dolomite), but it could also be rewritten for muscovite or phengite formation. The overall amount of phyllosilicate alteration will then be dependent on the amount of precursor clay minerals present in the host rock. In the Teena subbasin, it has not been possible to distinguish any extensive hydrothermal phyllosilicate alteration from the background diagenetic phyllosilicate formation. Furthermore, there is no independent evidence of a thermal anomaly that is associated with mineralized samples in the Lower HYC unit (e.g., elevated illite crystallinity).

Hanging-wall alteration. The nature of the alteration in the hanging-wall stratigraphy, which comprises the Lower and Middle HYC units, is far more cryptic than in the footwall. This asymmetry in alteration has previously been used to support SEDEX models but is clearly a feature of subseafloor replacement in the Teena subbasin. The depth at which mineralization in the Lower HYC unit was emplaced is constrained by the cryptic low-volume py2 disseminations and overgrowths among py1 that extend more than 200 m vertically above the Main lens (Magnall et al., 2020b; Hayward et al., 2021). The pyrite in the hanging-wall stratigraphy is progressively enriched in Tl and As toward the Main lens in the Lower HYC unit (Fig. 8C, D) and is likely to correspond with the distribution of py2.

The Tl and As enrichment in pyrite is the only evidence of hanging-wall alteration in the Teena subbasin. There are several possible reasons why lateral and hanging-wall alteration to Main lens in the Lower HYC unit is so cryptic:

1. Fluid infiltration into the hanging-wall sediments was likely restricted by sealing of feeder faults at this level, and by the relatively low permeability and low mechanical strength of the poorly lithified, pyritic, carbonaceous mudstone units of the Middle HYC unit, effectively forming an impermeable cap seal to the Lower HYC unit (Hayward et al., 2021).

2. Hydrothermal mass transfer in the Lower HYC unit would have been controlled by reaction permeability and disequilibrium between hydrothermal fluid and host rock. The lack of phyllosilicate alteration could be related to the efficiency of host-rock acid neutralization in a carbonate replacement system, which is effective in limiting mineralogical and lithogeochemical alteration footprints (Barker and Dipple, 2019).

3. Thermochemical sulfate reduction (TSR) may result in much less host-rock dissolution than might result from 2-component fluid mixing, in which reduced sulfur is derived from aqueous sulfide or sour gas (Corbella et al., 2004). Furthermore, experimental data has shown that at
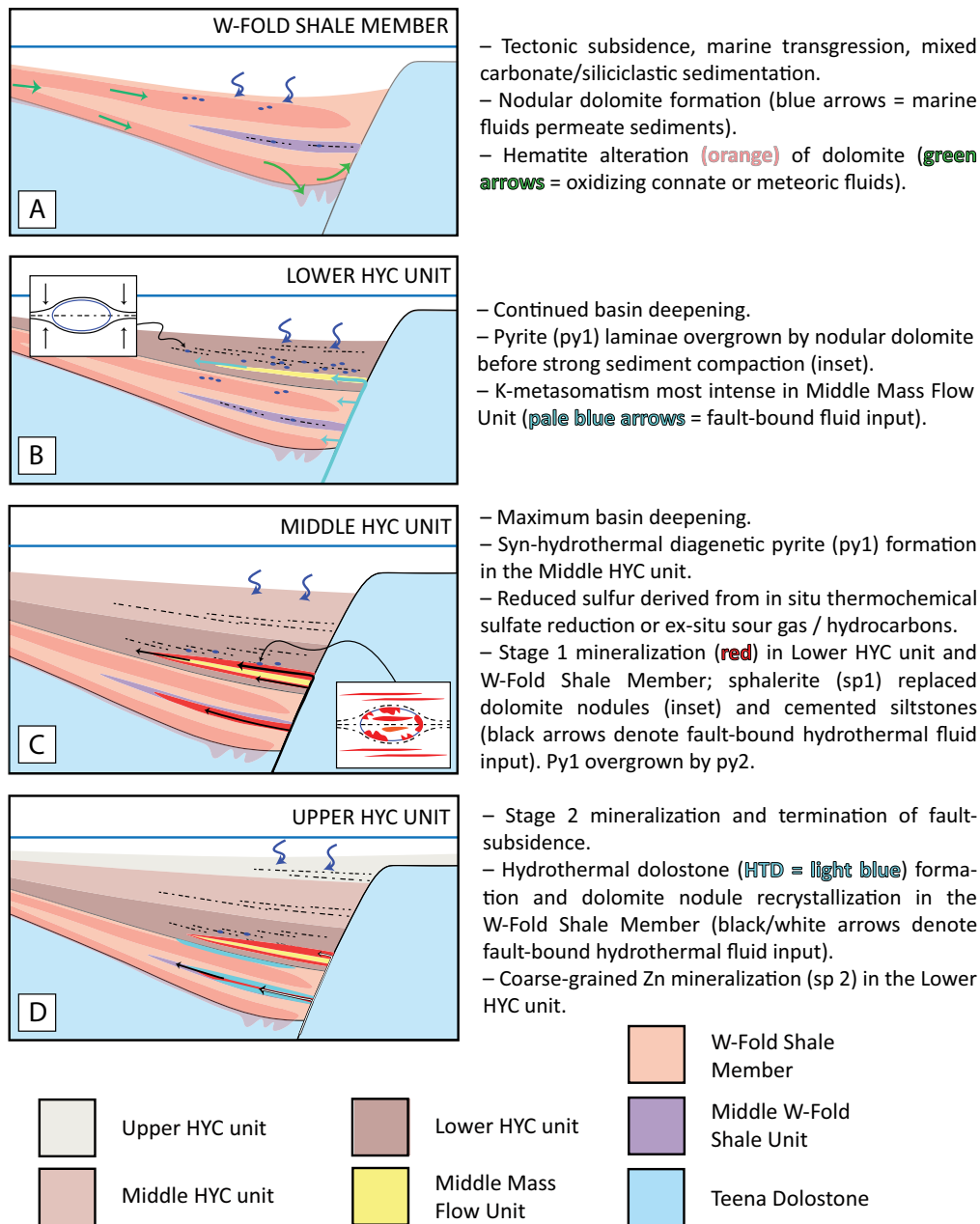
W-FOLD SHALE MEMBER

– Tectonic subsidence, marine transgression, mixed carbonate/siliciclastic sedimentation.
– Nodular dolomite formation (blue arrows = marine fluids permeate sediments).
– Hematite alteration (orange) of dolomite (green arrows = oxidizing connate or meteoric fluids).

A

LOWER HYC UNIT

– Continued basin deepening.
– Pyrite (py1) laminae overgrown by nodular dolomite before strong sediment compaction (inset).
– K-metasomatism most intense in Middle Mass Flow Unit (pale blue arrows = fault-bound fluid input).

B

MIDDLE HYC UNIT

– Maximum basin deepening.
– Syn-hydrothermal diagenetic pyrite (py1) formation in the Middle HYC unit.
– Reduced sulfur derived from in situ thermochemical sulfate reduction or ex-situ sour gas / hydrocarbons.
– Stage 1 mineralization (red) in Lower HYC unit and W-Fold Shale Member; sphalerite (sp1) replaced dolomite nodules (inset) and cemented siltstones (black arrows denote fault-bound hydrothermal fluid input). Py1 overgrown by py2.

C

UPPER HYC UNIT

– Stage 2 mineralization and termination of fault-subsidence.
– Hydrothermal dolostone (HTD = light blue) formation and dolomite nodule recrystallization in the W-Fold Shale Member (black/white arrows denote fault-bound hydrothermal fluid input).
– Coarse-grained Zn mineralization (sp 2) in the Lower HYC unit.

D

Legend:
- Upper HYC unit
- Middle HYC unit
- Lower HYC unit
- Middle Mass Flow Unit
- W-Fold Shale Member
- Middle W-Fold Shale Unit
- Teena Dolostone

Fig. 18. A summary of the diagenetic and hydrothermal events at progressive stages of subbasin evolution, in which (A)-(D) correspond with the deposition of the respective units (W-Fold Shale Member; Lower HYC, Middle, and Upper HYC units).

reasonable pore velocities (e.g., >20 m/yr) TSR can form a major Zn deposit (>3 Mt) in just 100,000 years (Thom and Anderson, 2008).

4. The metal-carrying capacity of the mineralizing fluids may have been considerably higher, invoking smaller fluid volumes than is commonly inferred in other less well-endowed basins from fluid inclusion studies of gangue minerals or from formation brine compositions (Wilkinson et al., 2009). The lack of a detectable thermal halo enveloping the hydrothermal mineralization and alteration would be consistent with lower flux rates of the hydrothermal fluid and efficient buffering by the wall rock.

Implications for exploration

The formation of sulfide mineralized rocks during midstage burial diagenesis means there is a diverse suite of eogenetic premineralization assemblages in both the foot- and hanging-wall stratigraphy at Teena (pyrite, dolomite, hematite, and authigenic K-feldspar). The distribution of these phases is unrelated to hydrothermal activity and represents open-system diagenetic mass transfer that was primarily controlled by tectonic subsidence and lateral facies variations in a shallow intercontinental setting (summarized in Fig. 18).

The tectonic subsidence initiated through growth fault activity resulted in an exceptionally thick hanging-wall sequence

in the Teena subbasin, in which the earliest generation of pyrite (py1) is most abundant and variably distributed (Figs. 4, 18). This early diagenetic pyrite is not directly associated with hydrothermal activity (Fig. 5), meaning the detection of pyrite under cover by regional electrical and gravimetric surveys only helps target a prospective subbasin depocenter and host facies, not necessarily a mineralization-related halo (e.g., Magnall et al., 2020b). On a much smaller scale, additional in situ trace element analyses of pyrite could help with further understanding the origin of trace element enrichment in the hanging-wall sequence at Teena and provide fertility and vectoring indicators to mineralized rocks.

The challenge for geoscientists exploring for CD-type Zn deposits in the McArthur Basin and elsewhere is in distinguishing synmineralization alteration from premineralization alteration assemblages, where the hanging-wall and lateral hydrothermal alteration halo can be much more subtle than burial diagenetic alteration. Exploration programs that use a broader basin analysis approach combined with detailed mapping of paragenetic and zonation relationships are recommended. Future studies may also benefit from the analysis of $\delta^{13}C$ and $\delta^{18}O$ values, which have potential to provide a much larger alteration footprint in the host rocks surrounding carbonate replacement systems (Barker and Dipple, 2019).

In the Teena subbasin, higher grade Zn mineralized rocks are not located within the most strongly reducing facies, nor the most carbonate-rich facies (Figs. 5, 18); rather, it has formed at the stratigraphic redox boundary between the generally oxidized footwall sequence (W-Fold Shale Member) and more reduced hanging-wall sequence (Lower HYC unit). Prospective subbasins should be identified on the basis of necessary lithofacies required for the development of a highly efficient metal trap. Requirements include a capacity for sulfate reduction, intraformational permeability and reactive host-rock replacement (carbonate facies), and proximity to feeder faults.

Conclusions

High-grade stratiform Zn mineralized lenses at the Teena deposit formed mostly via synextensional subseafloor replacement of dolomite during burial diagenesis. In the footwall and host stratigraphy, several low-temperature diagenetic mineral assemblages predated hydrothermal activity, are recognized regionally, and formed under open-system conditions during the main period of tectonic subsidence. In the main host unit, mass-flow volcaniclastic sandstone beds formed an aquifer for low-temperature K-rich saline fluids, which resulted in authigenic feldspar growth that occluded primary porosity. Petrographic data show that sulfide mineralization postdated all these early diagenetic assemblages and formed primarily via dolomite replacement (cement + nodules) and subordinate infill of pore spaces. Despite the protolith also having a high feldspar content, there was limited phyllosilicate alteration associated with sulfide mineralization. Furthermore, rather than forming within the most reducing facies, which are located within the hanging-wall stratigraphy, mineralized lenses are located at a stratigraphic redox boundary between the relatively oxidizing footwall and a more reducing mixed siliciclastic-dolomite host rock that was deposited during a major marine transgression.

Organic matter in the Teena subbasin is overmature, meaning that kerogen has undergone cracking to bitumen and gas. The timing of this cracking relative to hydrothermal mineralization is unclear, but it is notable that some of the fine-grained sphalerite cement formed in irregular interparticle micropore space that was likely to have previously been occupied by hydrocarbon phases (bitumen and gas). Tight lateral fluid flow and effective acid neutralization are the principal reasons why the hanging-wall hydrothermal alteration halo to the mineralized rocks is localized and relatively cryptic in the Teena subbasin.

The Teena deposit formed in a stratigraphic sweet spot where metal-bearing hydrothermal fluids first encountered lithologies that had potential for both carbonate dissolution and an effective reduction trap (S^{2-}). The identification of units containing a mixture of organic carbon and carbonate, which occur at favorable stratigraphic redox boundaries proximal to growth faults, is recommended for future exploration programs for this deposit type.

REFERENCES

Abad, I., 2007, Physical meaning and applications of the illite Kübler Index: Measuring reaction progress in low-grade metamorphism: Seminarios de la Sociedad Española de Mineralogía, v. 3, p. 53–64.

Ahmad, M., Dunster, J.N., and Munson, T.J., 2013, Chapter 15: McArthur Basin, in Ahmad, M., and Munson, T.J., comp., Geology and mineral resources of the Northern Territory: Northern Territory, Geological Survey, Special Publication 5.

Alonso-Azcarate, J., Barrenechea, J.F., Rodas, M., and Mas, J.R., 1995, Comparative study of the transition between very low-grade and low-grade metamorphism in siliciclastic and carbonate sediments: Early Cretaceous, Cameros Basin (northern Spain): Clay Minerals, v. 30, p. 407–419.

Barker, S.L.L., and Dipple, G.M., 2019, Exploring for carbonate-hosted ore deposits using carbon and oxygen isotopes: American Geophysical Union Monograph 242, p. 185–207.

Baruch, E.T., Kennedy, M.J., Löhr, S.C., and Dewhurst, D.N., 2015, Feldspar dissolution-enhanced porosity in Paleoproterozoic shale reservoir facies from the Barney Creek Formation (McArthur Basin, Australia): American Association of Petroleum Geologists Bulletin, v. 99, p. 1745–1770.

Battaglia, S., Leoni, L., and Sartori, F., 2004, The Kübler index in late diagenetic to low-grade metamorphic pelites: A critical comparison of data from 10 Å and 5 Å peaks: Clays and Clay Minerals, v. 52, p. 85–105.

Beaufort, D., Rigault, C., Billon, S., Billault, V., Inoue, A., Inoue, S., and Patrier, P., 2015, Chlorite and chloritization processes through mixed-layer mineral series in low-temperature geological systems—a review: Clay Minerals, v. 50, p. 497–523.

Bernard, S., and Horsfield, B., 2014, Thermal maturation of gas shale systems: Annual Review of Earth and Planetary Sciences, v. 42, p. 635–651.

Betts, P.G., Giles, D., and Lister, G.S., 2003, Tectonic environment of shale-hosted massive sulfide Pb-Zn-Ag deposits of Proterozoic northeastern Australia: Economic Geology, v. 98, p. 557–576.

Betts, P.G., Giles, D., Mark, G., Lister, G.S., Goleby, B.R., and Aillères, L., 2006, Synthesis of the Proterozoic evolution of the Mt. Isa inlier: Australian Journal of Earth Sciences, v. 53, p. 187–211.

Betts, P.G., Armit, R.J., Stewart, J., Aitken, A.R.A., Ailleres, L., Donchak, P., Hutton, L., Withnall, I., and Giles, D., 2016, Australia and Nuna: Geological Society (London) Special Publication v. 424, p. 47–81.

Bjørlykke, K., 1998, Clay mineral diagenesis in sedimentary basins—a key to the prediction of rock properties. Examples from the North Sea Basin: Clay Minerals, v. 33, p. 15–34.

——2014, Relationships between depositional environments, burial history and rock properties. Some principal aspects of diagenetic process in sedimentary basins: Sedimentary Geology, v. 301, p. 1–14.

Bjørlykke, K., and Jahren, J., 2012, Open or closed geochemical systems during diagenesis in sedimentary basins: Constraints on mass transfer during diagenesis and the prediction of porosity in sandstone and carbonate reservoirs: American Association of Petroleum Geologists Bulletin, v. 96, p. 2193–2214.

Blevings, S.K., Kraft, J.L., Stemler, J.U., and Krolak, T.E., 2013, An overview of the structure, stratigraphy, and Zn-Pb-Ag deposits of the Red Dog district, northwestern Alaska: Society of Economic Geologists, Special Publication 17, p. 361–387.

Broadbent, G.C., Myers, R.E., and Wright, J.V, 1998, Geology and origin of shale-hosted Zn-Pb-Ag mineralization at the Century deposit, northwest Queensland, Australia: Economic Geology, v. 93, p. 1264–1294.

Burley, S.D., Kantorowicz, J.D., and Waugh, B., 1985, Clastic diagenesis: Geological Society, London, Special Publication 18, p. 189–226.

Corbella, M., Ayora, C., and Cardellach, E., 2004, Hydrothermal mixing, carbonate dissolution and sulfide precipitation in Mississippi Valley-type deposits: Mineralium Deposita, v. 39, p. 344–357.

Crick, I.H., Boreham, C.J., Cook, A.C., and Powell, T.G., 1988, Petroleum geology and geochemistry of Middle Proterozoic McArthur Basin, northern Australia II: Assessment of source rock potential: American Association of Petroleum Geologists Bulletin, v. 72, p. 1495–1514.

Davidson, G.J., 1999, Feldspar metasomatism along a Proterozoic rift-basin margin—"Smoke" around a base-metal "fire" (HYC deposit, Australia) or a product of background diagenesis?: Bulletin of the Geological Society of America, v. 111, p. 663–673.

Davidson, G.J., and Dashlooty, S.A., 1993, The Glyde sub-basin: A volcaniclastic-bearing pull-apart basin coeval with the McArthur River base-metal deposit, Northern Territory: Australian Journal of Earth Sciences, v. 40, p. 527–543.

Ehrenberg, S.N., 2006, Porosity destruction in carbonate platforms: Journal of Petroleum Geology, v. 29, p. 41–52.

Eldridge, C.S., Williams, N., and Walshe, J.L., 1993, Sulfur isotope variability in sediment-hosted massive sulfide deposits as determined using the ion microprobe SHRIMP: II. A study of the H.Y.C.deposit at McArthur River, Northern Territory, Australia: Economic Geology, v. 88, p. 1–26.

Goodfellow, W.D., 1987, Anoxic stratified oceans as a source of sulphur in sediment-hosted stratiform ZnPb deposits (Selwyn Basin, Yukon, Canada): Chemical Geology: Isotope Geoscience Section, v. 65, p. 359–382.

Goodfellow, W.D., and Lydon, J.W., 2007, Sedimentary exhalative (SEDEX) deposits: Geological Association of Canada, Special Publication no. 5, p. 163–183.

Goodfellow, W.D., Lydon, J.W., and Turner, R.J., 1993, Geology and genesis of stratiform sediment-hosted (SEDEX) zinc-lead-silver sulphide deposits: Geological Association of Canada, Special Paper 40, p. 201–252.

Grant, J.A., 1986, The isocon diagram—a simple solution to Gresens' equation for metasomatic alteration: Economic Geology, v. 81, p. 1976–1982.

Grondijs, H.F., and Schouten, C., 1937, A study of the Mount Isa ores: Economic Geology, v. 32, p. 407–450.

Hayward, N., Magnall, J.M., Taylor, M., King, R., McMillan, N., and Gleeson, S.A., 2021, The Teena Zn-Pb deposit (McArthur Basin, Australia). Part I: Syndiagenetic base metal sulfide mineralization related to dynamic sub-basin evolution: Economic Geology, v. 116, p. XX.

Helgeson, H.C., Knox, A.M., Owens, C.E., and Shocks, E.L., 1993, Petroleum, oil field waters, and authigenic mineral assemblages: Are they in metastable equilibrium in hydrocarbon reservoirs?: Geochemica et Cosmochemica Acta, v. 57, p. 3295–3339.

Hinman, M.C., 2001, Inhilation, thermochemical sulphate reduction, and processes of ore formation at McArthur River, Northern Territory: James Cook University of North Queensland, A Hydrothermal Odyssey Ore Deposits Conference, Townsville, Australia, Poster presentation.

Hood, A.V.S., Wallace, M.W., and Drysdale, R.N., 2011, Neoproterozoic aragonite-dolomite seas? Widespread marine dolomite precipitation in Cryogenian reef complexes: Geology, v. 39, p. 871–874.

Hornibrook, E.R.C., and Longstaffe, F.J., 1996, Berthierine from the Lower Cretaceous Clearwater Formation, Alberta, Canada: Clays and Clay Minerals, v. 44, p. 1–21.

Hower, J., Eslinger, E.V., Hower, M.E., and Perry, E.A., 1976, Mechanism of burial metamorphism of argillaceos sediment: Geological Society Of America Bulletin, v. 87, p. 725–737.

Humphris, S.E., Alt, J.C., Teagle, D.A.H., and Honnorez, J.J., 1998, Geochemical changes during hydrothermal alteration of basement in the stockwork beneath the active TAG hydrothermal mound: Proceedings of the Ocean Drilling Program: Scientific Results, v. 158, p. 255–276.

Ireland, T., Large, R.R., McGoldrick, P., and Blake, M., 2004, Spatial distribution patterns of sulfur isotopes, nodular carbonate, and ore textures in the McArthur River (HYC) Zn-Pb-Ag deposit, Northern Territory, Australia: Economic Geology, v. 99, p. 1687–1709.

Jackson, M.J., Muir, M.D., and Plumb, K.A., 1987, Geology of the southern McArthur Basin, in Jackson, M.J., Muir, M.D., and Plumb, K.A., eds., Northern Territory: Canberra, Australian Government, 173 p.

Jarvie, D.M., Hill, R.J., Ruble, T.E., and Pollastro, R.M., 2007, Unconventional shale-gas systems: The Mississippian Barnett Shale of north-central Texas as one model for thermogenic shale-gas assessment: American Association of Petroleum Geologists Bulletin, v. 91, p. 475–499.

Johnson, B.R., Tostevin, R., Gopon, P., Wells, J., Robinson, S.A., and Tosca, N.J., 2020, Phosphorus burial in ferruginous SiO_2-rich Mesoproterozoic sediments: Geology, v. 48, p. 92–96.

Kunzmann, M., Schmid, S., Blaikie, T.N., and Halverson, G.P., 2019, Facies analysis, sequence stratigraphy, and carbon isotope chemostratigraphy of a classic Zn-Pb host succession: The Proterozoic middle McArthur Group, McArthur Basin, Australia: Ore Geology Reviews, v. 106, p. 150–175.

Large, R.R., Bull, S.W., Cooke, D.R., and McGoldrick, P.J., 1998, A genetic model for the HYC deposit, Australia: Based on regional sedimentology, geochemistry, and sulfide-sediment relationships: Economic Geology, v. 93, p. 1345–1368.

Large, R.R., Bull, S.W., McGoldrick, P.J. and Walters, S.G., 2005, Stratiform and strata-bound Zn-Pb-Ag deposits in Proterozoic sedimentary basins, northern Australia: Economic Geology, v. 100, p. 931–963.

Lynch, L.E.O., 1997, Frio shale mineralogy and the stoichiometry of the smectite-to-illite reaction: The most important reaction in clastic sedimentary diagenesis: Clays and Clay Minerals, v. 45, p. 618–631.

Magnall, J.M., Gleeson, S.A., Poulton, S.W., Gordon, G.W., and Paradis, S., 2018, Links between seawater paleoredox and the formation of sediment-hosted massive sulphide (SHMS) deposits—Fe speciation and Mo isotope constraints from Late Devonian mudstones: Chemical Geology, v. 490, p. 45–60.

Magnall, J.M., Gleeson, S.A., and Paradis, S., 2020b, A new subseafloor replacement model for the Macmillan Pass clastic-dominant Zn-Pb ± Ba deposits (Yukon, Canada): Economic Geology, v. 115, p. 953–959.

Magnall, J.M., Gleeson, S.A., Hayward, N., and Rocholl, A., 2020a, Massive sulfide Zn deposits in the Proterozoic did not require euxinia: Geochemical Perspectives Letters, v. 13, p. 19–24.

Magnall, J.M., Gleeson, S.A., Hayward, N., and Dalrymple, I., 2021, Major, minor, and trace element lithogeochemistry of the Barney Creek Formation, Carpentaria Province northern Australia: Accessed at https://doi.org/10.5880/GFZ.3.1.2021.001.

Martel, E., 2017, The importance of structural mapping in ore deposits—a new perspective on the Howard's Pass Zn-Pb district, Northwest Territories, Canada: Economic Geology, v. 112, p. 1285–1304.

McGoldrick, P., Winefield, P., Bull, S., Selley, D., and Scott, R., 2010, Sequences, synsedimentary structures, and sub-basins: The where and when of SEDEX zinc systems in the southern McArthur Basin, Australia: Economic Geology Special Publication 15, p. 367–389.

McKinley, J.M., Worden, R.H., and Ruffell, A.H., 2009, Smectite in sandstones: A review of the controls on occurrence and behaviour during diagenesis, in Morad, S., and Worden, R., eds., Clay mineral cements in sandstones: Blackwell Publishing Ltd., p. 109–128.

Merriman, R.J., 2005, Clay minerals and sedimentary basin history: European Journal of Mineralogy, v. 17, p. 7–20.

Merriman, R.J. and Peacor, D., 1999, Very low-grade metapelites: Mineralogy, microfabrics and measuring reaction progress, in Frey, M., and Robinson, D. eds., Low grade metamorphism: Blackwell Science Ltd., p. 10–60.

Meunier, A., 2005, Diagenesis and very low grade metamorphism: Berlin, Springer, Clays, p. 329–377.

Milliken, K., 2003, Late diagenesis and mass transfer in sandstone shale sequences: Treatise on Geochemistry, v. 7, p. 159–190.

Morad, S., Ketzer, J.M., and De Ros, L.R., 2000, Spatial and temporal distribution of diagenetic alterations in siliciclastic rocks: Implications for mass transfer in sedimentary basins: Sedimentology, v. 47, p. 95–120.

Mudd, G.M., Jowitt, S.M., and Werner, T.T., 2017, The world's lead-zinc mineral resources: Scarcity, data, issues and opportunities: Ore Geology Reviews, v. 80, p. 1160–1190.

Mukherjee, I., and Large, R., 2017, Application of pyrite trace element chemistry to exploration for SEDEX style Zn-Pb deposits: McArthur Basin, Northern Territory, Australia: Ore Geology Reviews, v. 81, p. 1249–1270.

Nieto, F., Velilla, N., Peacor, D.R., and Huertas, M.O., 1994, Regional retrograde alteration of sub-greenschist facies chlorite to smectite: Contributions to Mineralogy and Petrology, v. 115, p. 243–252.

Page, R.W., and Sweet, I.P., 1998, Geochronology of basin phases in the western Mt. Isa inlier, and correlation with the McArthur Basin: Australian Journal of Earth Sciences, v. 45, p. 219–232.

Page, R.W., Jackson, M.J., and Krassay, A.A., 2000, Constraining sequence stratigraphy in north Australian basins: SHRIMP U-Pb zircon geochronology between Mt. Isa and McArthur river: Australian Journal of Earth Sciences, v. 47, p. 431–459.

Plumb, K.A., 1979, The tectonic evolution of Australia: Earth Science Reviews, v. 14, p. 205–249.

Rafiei, M., and Kennedy, M., 2019, Weathering in a world without terrestrial life recorded in the Mesoproterozoic Velkerri Formation: Nature Communications, v. 10.

Rawlings, D.J., 1999, Stratigraphic resolution of a multiphase intra-cratonic basin system: The McArthur Basin, northern Australia: Australian Journal of Earth Sciences, v. 46, p. 703–723.

Reynolds, M.A., Gingras, M.K., Gleeson, S.A., and Stemler, J.U., 2015, More than a trace of oxygen: Ichnological constraints on the formation of the giant Zn-Pb-Ag ± Ba deposits, Red Dog district, Alaska: Geology, v. 43, p. 867–870.

Rieger, P., Magnall, J.M., Gleeson, S.A., Schleicher, A.M., Bonitz, M., and Lilly, R., 2021, The mineralogical and lithogeochemical footprint of the George Fisher Zn-Pb-Ag massive sulphide deposit in the Proterozoic Urquhart Shale Formation, Queensland, Australia: Chemical Geology, v. 560, p. 119975.

Schmidt, V., and McDonald, D.A., 1979, The role of secondary porosity in the course of sandstone diagenesis: Society of Economic Paleontologists and Mineralogists (SEPM) Special Publication, v. 26, p. 175–207.

Scrimgeour, I.R. 2006, The Arunta Region: links between tectonics and mineralization, *in* Munson, T.J., and Scrimgeour, I.S., eds., Annual Geoscience Exploration Seminar (AGES). 2006. Record of abstracts: Northern Territory Geological Survey Record 2006-002, p. 7–10.

Smith, J.T., and Ehrenberg, S.N., 1989, Correlation of carbon dioxide abundance with temperature in clastic hydrocarbon reservoirs: Relationship to inorganic chemical equilibrium: Marine and Petroleum Geology, v. 6, p. 129–135.

Southgate, P.N., Bradshaw, B.E., Domagala, J., Jackson, M.., Idnurm, M., Krassay, A.A., Page, R.W., Sami, T.T., Scott, D.L., Lindsay, J.F., McConachie, B.M., and Tarlowski, C.Z., 2000, Chronostratigraphic framework for Palaeoproterozoic rocks (1730-1575Ma) in northern Australia and their implications for base-metal mineralisation: Australian Journal of Earth Sciences, v. 47, p. 461–483.

Spinks, S.C., Pearce, M.A., Liu, W., Kunzmann, M., Ryan, C.G., Moorhead, G.F., Kirkham, R., Blaikie, T., Sheldon, H.A., Schaubs, P.M., and Rickard, W.D.A., 2021, Carbonate replacement as the principal ore formation process in the Proterozoic McArthur River (HYC) sediment-hosted Zn-Pb deposit, Australia: Economic Geology, v. 116, p. 1–26.

Śródoń, J., 1999, Nature of mixed-layer clays and mechanisms of their formation and alteration: Annual Review of Earth and Planetary Sciences, v. 27, p. 19.

Tang, D., Shi, X., Jiang, G., Zhou, X., and Shi, Q., 2017, Ferruginous seawater facilitates the transformation of glauconite to chamosite: An example from the Mesoproterozoic Xiamaling Formation of North China: American Mineralogist, v. 102, p. 2317–2332.

Thom, J., and Anderson, G.M., 2008, The role of thermochemical sulfate reduction in the origin of Mississippi Valley-type deposits. I. Experimental results: Geofluids, v. 8, p. 16–26.

Tucker, M.E., 1982, Precambrian dolomites: Petrographic and isotopic evidence that they differ from Phanerozoic dolomites.: Geology, v. 10, p. 7–12.

Turner, R.J.W., 1992, Formation of Phanerozoic stratiform sediment-hosted zinc-lead deposits: Evidence for the critical role of ocean anoxia: Chemical Geology, v. 99, p. 165–188.

Warr, L.N., and Cox, S.C., 2016, Correlating illite (Kübler) and chlorite (Árkai) "crystallinity" indices with metamorphic mineral zones of the South Island, New Zealand: Applied Clay Science, v. 134, p. 164–174.

Warr, L.N., and Rice, A.H.N., 1994, Interlaboratory standardization and calibration of day mineral crystallinity and crystallite size data: Journal of Metamorphic Geology, v. 12, p. 141–152.

Weaver, C.E., 1960, Possible uses of clay minerals in the search for oil: American Association of Petroleum Geologists Bulletin, p. 1505–1518.

Whitbread, M.A., 2004, Lithogeochemical alteration around the Century and Elura Zn-Pb-Ag deposits: Detecting alteration expressions in the deep and near surface environments: University of Canberra, 410 p.

Wilkinson, J.J., Stoffell, B., Wilkinson, C.C., Jeffries, T.E., and Appold, M.S., 2009, Anomalously metal-rich fluids form hydrothermal ore deposits: Science, v. 323, p. 764–767.

Wilkinson, J.J., Crowther, H.L., and Coles, B.J., 2011, Chemical mass transfer during hydrothermal alteration of carbonates: Controls of seafloor subsidence, sedimentation and Zn-Pb mineralization in the Irish Carboniferous: Chemical Geology, v. 289, p. 55–75.

Williams, N., 1978, Studies of the base metal sulfide deposits at McArthur River, Northern Territory, Australia: I. The Cooley and Ridge deposits: Economic Geology, v. 73, p. 1005–1035.

Worden, R.H., and Burley, S.D., 2003, Sandstone diagenesis: The evolution of sand to stone, *in* Burley, S.D., and Worden, R.H., eds., Sandstone Diagenesis: Wiley, International Association of Sedimentologists, p. 1–44.

Joe Magnall is a postdoctoral research scientist at the GFZ Helmholtz Centre in Potsdam (Germany). Before moving to Germany, Joe completed his B.Sc. (environmental geology) and M.Sc. (geochemistry) at the University of Leeds (UK) and his Ph.D. at the University of Alberta (Canada). Joe's research is primarily focused toward developing a better understanding of some of the fundamental aspects of sediment-hosted mineral systems, including the temporal and spatial distribution of deposits and the specific parameters that control the formation of high-grade systems. Up to this point, Joe has worked on deposits from world-class Zn districts in the Canadian Cordillera and northern Australia and typically enjoys combining field geology, petrographic techniques, and multiple types of geochemical data.